Microstructural Study of Zirconium Oxide Grown on a Zirconium Alloy Substrate for Orthopaedic Applications

by

Stephan P. Mangin

Diplome d'Ingenieur
Ecole Centrale de Lyon, 1995

Submitted to the Department of Materials Science and Engineering
in Partial Fulfillment of the Requirements for the Degree of

Master of Science
in Materials Science and Engineering

at the

MASSACHUSETTS INSTITUTE OF TECHNOLOGY

JUNE 1998

© 1998 Massachusetts Institute of Technology. All rights reserved.

Signature of author _____
Department of Materials Science and Engineering
May 8,1998

Certified by _____
Linn W. Hobbs
John F. Elliott Professor of Materials
Thesis Supervisor

Accepted by _____
Linn W. Hobbs
John F. Elliott Professor of Materials
Chairman, Department Committee on Graduate Students

MASSACHUSETTS INSTITUTE OF TECHNOLOGY

JUN 24 1998

Science

LIBRARIES

For Howard Nalt.

Microstructural Study of Zirconium Oxide Grown on a Zirconium Alloy Substrate for Orthopaedic Applications

by

Stephan P. Mangin

Submitted to the Department of Materials Science and Engineering
on May 8, 1998 in Partial Fulfillment of the
Requirements for the Degree of Master of Science
in Materials Science and Engineering.

ABSTRACT

An experimental study was performed on the microstructure of an oxide layer grown on a zirconium alloy substrate containing 2.5 weight percent niobium. The purpose of this layer is to protect the load bearing surface of a hip or knee prosthesis made of the zirconium alloy.

Electron microscopy, principally transmission electron microscopy was used to assess the microstructures and microstructural development of the scale on the underlying alloy substrate. A special specimen preparation method was developed for study of cross-sections. Observations showed that the oxide was almost entirely monoclinic ZrO_2 with a columnar morphology from the scale surface to the interface with the alloy, and crystallographically textured. Different substrate orientation and oxidation conditions resulted in minor changes in oxide morphologies. Defect regions found in the scale attributed to oxidation of a Nb-rich alloy phase. All the niobium content of the alloy can be accomodated in solid solution within the monoclinic zirconia scale phase, with additions of a possible $6ZrO_2.Nb_2O_5$ phase for oxidation of alloy regions locally enriched in niobium.

Thesis Supervisor: Linn W. Hobbs
Title: John F. Elliott Professor of Materials

Table of Contents

List of Figures

List of Tables

List of Abbreviations used

bcc	body-centered-cubic
CVD	chemical vapor deposition
ESEM	environmental scanning electron microscopy
hcp	hexagonal-close-packed
HA	hydroxyapatite
PVD	plasma vapor deposition
PMMA	poly methyl methacrylate acetylene
STEM	scanning transmission electron microscopy
TEM	transmission electron microscopy
UHMWPE	ultrahigh-molecular-weight polyethylene
YPSZ	yttria partially stabilized zirconia

Acknowledgments

I would like to thank the people whose help was essential to complete this work:
Professor Linn W. Hobbs -- who supported and guided me all along this project, and introduced me to the field of electron microscopy.
Smith & Nephew Inc., Orthopaedics Division, and their representative Dr. Gordon Hunter -- who initiated and supported the project.
My colleagues Valarie Benezra and Dr. Meri Treska who introduced me to the experimental techniques presented here, particularly procedures for TEM sample preparation and observation.
Mike Frongillo, Dr. David Bell, Dr. Tony Garratt-Reed of the CMSE Electron Microscopy Central Facility, for introducing me to and assisting me with the operation of electron microscopes.

I would like to thank Howard Nalt for his moral support and consistent encouragement.

Finally, I would like to thank my parents, Pierre and Mary-Claire Mangin.

Chapter 1:

Introduction

Zirconium alloys are used extensively in the nuclear industry because they have a small neutron absorption cross-section [22]. The possible formation of a highly protective oxide scale on their surface has added to their attractiveness. Several types of zirconium alloys and their corrosion behaviour have been investigated [26-29]. Among them are alloys with added niobium, and, more specifically, zirconium alloys containing 2.5wt% niobium were chosen for pressure tubes in Canadian CANDU nuclear reactors.

In orthopaedic applications, this Zr-2.5wt%Nb alloy with an oxidized surface could offer the advantage of improving wear performance in the contact area of an articulated implant. Alloys currently commercially in joint applications, such as Co-Cr and Ti-Al-V, have to maintain wear resistance over milllions of articulation cycles. Oxidation of Zr-2.5wt%Nb alloys results in a protective oxide layer whose internal microstructure and interface with the metal confer superior wear resistance. The oxide grain orientation, presence of defects, and phases present in the oxide all influence wear and spalling behaviour. Because the role of microstructure is so critical, electron microscopy is the appropriate tool to conduct this study. Observations with transmission electron microscopy (TEM) and scanning transmission electron microscopy (STEM) were made across both the oxide and the alloy, to understand what transformation mechanisms guide the growth of the oxide, and to detect potential flaws in the scale and at the interface. The influence of substrate orientation and process conditions was also studied. Additional observations were made using environmental scanning electron microscopy (ESEM).

Chapter 2:

Research context

2.1. Biomaterials for orthopaedic applications.

Essential orthopaedic materials properties.

The performance of prostheses depends on the properties of the materials used, the design of the device, and the method of fixation (that is, attachment to the musculoskeletal system) [3]. Figures 2.1 and 2.2 shows examples of hip and knee prostheses. The hip prosthesis consists typically of a femoral component with a spherical head articulating on a proximal cup. The lower part or stem of the femoral component is implanted into the femur. The knee prosthesis consists typically of a femoral part articulating over a tibial plateau. The articulation surfaces consist typically of a metal surface (femoral components for hip and knee prostheses) on a ultrahigh-molecular-weight polyethylene (UHMWPE) surface (acetabular or tibial component of a knee prosthesis, and proximal component or cup of a hip prosthesis). The fixation surfaces of the hip or knee prostheses on bone are variable. For the hip proximal component and the two knee components, the initial fixation is ensured by bone screws. The stem of the hip femoral component can be inserted directly inside the femoral bone by press-fit adherence, or using a polymerized cement PMMA (poly methyl methacrylate acetylene). These options divide the hip implants into two categories: the first group are cementless implants, the second cemented ones. Material properties consist of mechanical characteristics such as strength and modulus of elasticity, tribologic features including wear, resistance to degradation (for example, corrosion), and biocompatibility [3].

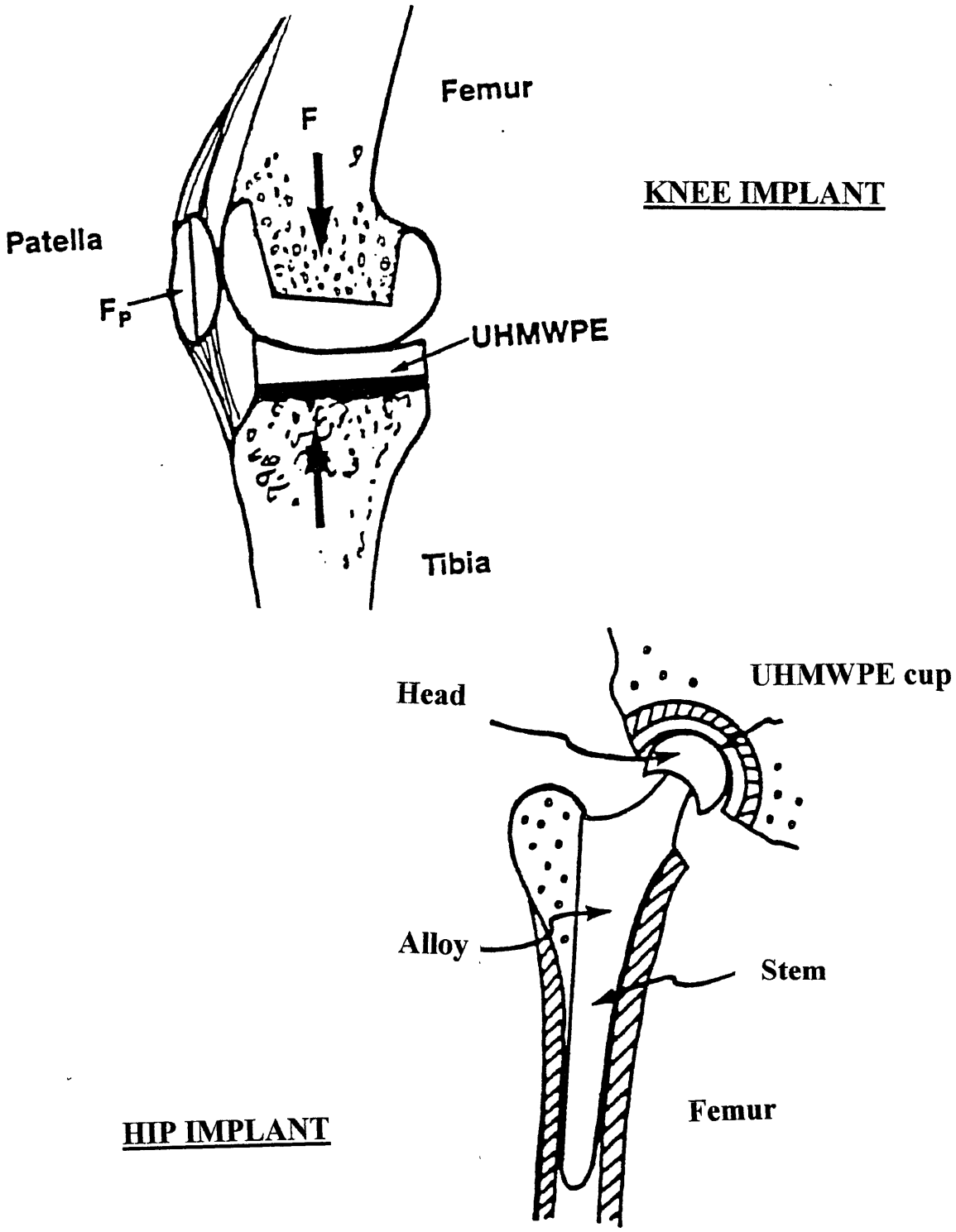

Figure 2.1: Schematic illustration of total hip and knee implants [9].

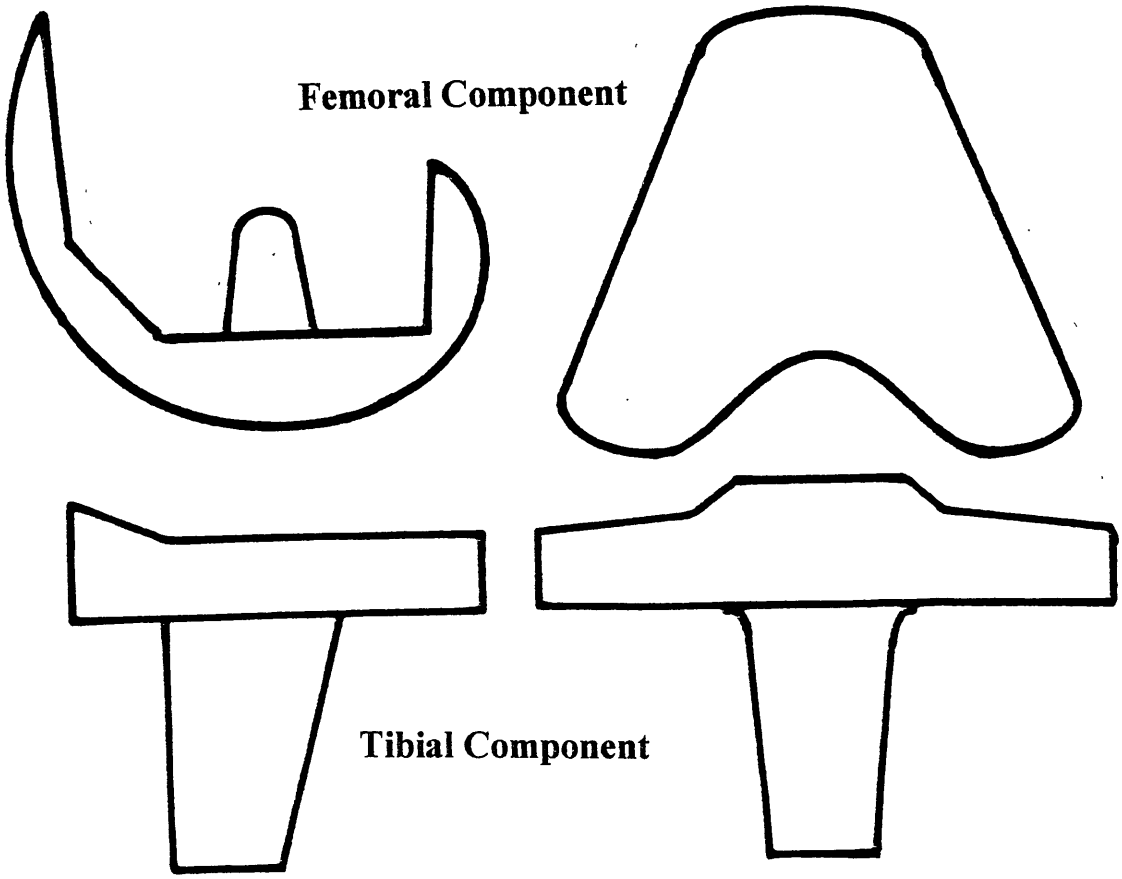

Figure 2.2: Schematic profile views of total knee prosthesis [6]

Issues for currently-used orthopaedic materials.

Metals are currently the most Food and Drug Administration (FDA)-approved and commercially used materials for hip and knee prostheses: their high strength and toughness eliminates the concerns about breakage in service. Cobalt-chromium alloys have gained wide recognition because of their high strength, but also their relative biocompatibility, although the release of Cr^{6+} toxic metal ions in the tissues is a serious concern [5]. The titanium Ti-6Al-4V (6% aluminum and 4% vanadium) alloy has received increased interest because of its chemical inertia in tissues and the resulting decreased ion release. However, it exhibits an inconveniently low wear-resistance. For any innovative biomaterial proposed for hip or knee replacement, its ability to resist wear is essential. The debris generated by wear, either from the metal or the polyethylene (or debris that becomes embedded in the polyethylene), promotes inflammatory processes that involve the release by cells of regulators triggering bone resorption around the implant. Bone loss after total knee arthroplasty has been observed [6,7] in the short term on patients, and bone failure is likely to happen in the long term with longer periods of cyclic loading. Furthermore, as a result of bone loss, revision arthroplasty is compromised.

Wear is, indeed, the factor limiting the life of total joint replacement prostheses; it can be found on the articulating surfaces (cyclic movements), or on fixation portions of the implant surrounded by bone or bone cement (micromotion causing fretting wear). Polyethylene is the main source of wear particles; it is considered that, while acetabular cups (for the hip) undergo adhesive and abrasive wear, tibial components (for the knee) undergo fatigue and abrasive wear [4]. However, metal and cement particles also play a major role in three-body wear and body inflammatory responses. As a result, wear testing for orthopaedic applications is an extensive experimental procedure. The tribological properties of a metal or coating surface on UHMPE or PMMA can be evaluated using a pin-on disc apparatus [8]. From such measurements, the coefficients of friction and wear rates can be inferred. The attachment of a coating (or passivation layer for a metal surface) can be evaluated by a scratch test. Eventually, the conditions of loading on the wear surfaces in the human body are simulated on the actual device (e.g. hip or knee

prosthesis) by an apparatus applying cyclic loading [13]. The loads are applied over millions of cycles, which represent the amount of loading an implanted device has to withstand over its expected lifetime of 10 to 25 years.

Value of oxidized zirconium alloy in orthopaedics.

One of the current challenges is to improve the wear-resistance of orthopaedic material bearing surfaces, for which purpose various surface coating methods are being investigated [9]. These coatings include plasma-sprayed alumina and zirconia, TiN and amorphous diamond-like coatings applied via PVD/CVD (plasma vapor deposition/ chemical vapor deposition) methods. Several surface hardening treatments, such as nitrogen ion implantation, are used to improve the titanium alloy wear properties. Diffusion of oxygen into the zirconium alloy increases the hardness of the substrate, improving the wear properties of the metal [10]. For hip replacement, femorals heads made of ceramic (alumina and zirconia) materials are widely used for their excellent tribology properties [9]. Experimentally, a 3-4 μm ZrO_2 surface layer can not only withstand ten million abrasion cycles against PMMA bone cement, but also shows no indication of surface roughening [1]. The friction against UHMWPE and accompanying wear for the zirconia surface is shown in figure 2.3 [1] in comparison to those for cast Co-Cr-Mo with a similar surface finish. The relative reduction in UHMWPE wear with ZrO_2 surfaces is also consistant with hip simulator wear results [1]. Other comparative studies on wear of zirconia surfaces in artificial hip and knee joint simulators have shown encouraging properties [12,14]. Oxidation of zirconium alloys may therefore represent a valuable surface-treatment method, and particularly could render the zirconium alloy as an optimal biomaterial for orthopaedic applications.

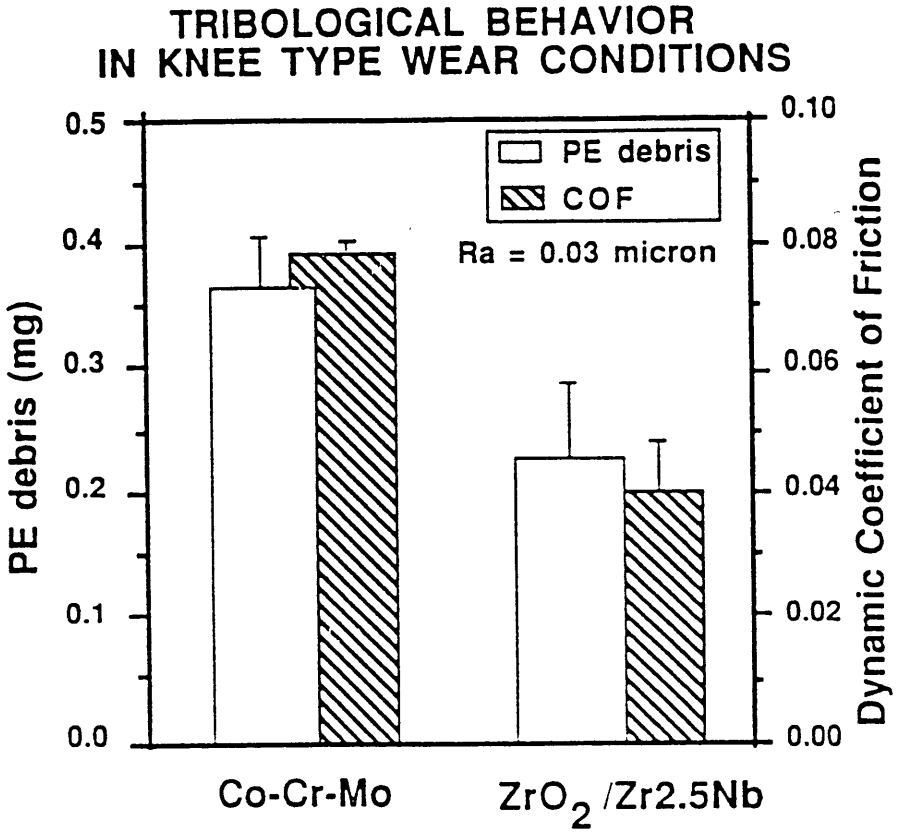

Figure 2.3: Tribological behaviour of oxidized zirconium in knee-type wear conditions [1]

Toxicity and biocompatibility of oxidized zirconium for orthopaedic applications.

Other properties essential for biomaterials are good resistance to degradation and biocompatibility. The electrochemical behaviour of oxidized zirconium, related to its corrosion and biocompatibility performances, has been studied and found promising [18]. Aging of zirconia ceramics has been studied *in vivo* and *in vitro*, and the oxide showed no degradation or loss of strength after 2 years [16]. The reaction of tissue cells to yttria partially stabilized zirconia (YPSZ, commercial zirconia) has been evaluated *in vivo* using histomorphometry [17].

Among the main issues for implanted materials is the bone response. The capacity of bone to heal or regenerate at the interface with the implant surface (see figure 2.1) will largely control whether the biomaterial is suitable for cementless or cemented applications. For cementless applications, various forms of surface processing are currently used to avoid loosening, micromotion, and wear at the implant-bone interface. These processing forms promote bone ingrowth or even bone bonding to the implant surface: they can consist of macrotexturing, or microtexturing (such as grit-blasting), which roughen the implant surface, or coating with hydroxyapatite (HA), a mineral material promoting bone regeneration and fixation. Zr-2.5Nb alloy was found to have a bone response similar or superior to Co-Cr alloy (the common reference alloy) when implanted in the rabbit tibia model [19,20]. These discoveries present the possibility of creating a cementless femoral component by abrading an oxidized zirconium-alloy component to expose the metal substrate along the attachment portion, while leaving the oxide across the articulating surface. Finally the *in vitro* tribology study of oxidized zirconium articulation against bovine articular cartilage [21] showed the suitability of zirconium as the bearing surface for hip arthroplasty. The use of this material for cementless prostheses (direct contact between bone and the implant, no use of PMMA cement for fixation) appears therefore possible.

As a conclusion, oxidized zirconium displays a range of properties that makes it an attractive candidate for various orthopaedic applications such as hip an knee prostheses.

2.2 Zirconium alloys.

Several types of zirconium alloys have been investigated and used industrially. One important application is the use of zirconium alloys in nuclear reactors. Indeed, zirconium presents the advantage of having a particularly small neutron absorption cross-section. Among alloys investigated are zircalloy and zirconium alloys with added niobium [22,24,26-29]. Zircalloy-4, used for fuel cladding tubes, has a nominal composition (wt%) of Zr-1.50Sn-0.19Fe-0.10Cr-1280ppmO-30ppmH [22]. Investigated alloys containing niobium are: Zr-19wt%Nb [28], Zr-20wt%Nb [29], and Zr-2.5wt%Nb [24]. The phase diagram of niobium-zirconium (figure 5.2, [32]) indicates a eutectoid reaction at 625° C. Zr-2.5wt%Nb alloys are used for pressure tubes in Canadian CANDU reactors.

Lin [24] has described the microstructure of Zr-2.5wt%Nb alloy: it consists of highly elongated grains of hexagonal-close-packed (hcp) α-Zr (containing ~1% Nb), typically 0.3-0.5 μm thick, surrounded by thin sheaths of body-centered-cubic (bcc) β-Zr (containing ~20% Nb). The β-Zr phase is metastable and will transform eventually to the equilibrium β-Nb phase (~85% Nb) as described in the phase diagram. All these alloys used in the nuclear industry are prepared under specific conditions, such a stress relief treatments, or high-temperature treatments in steam. These all account for particular alloy microstructures. Also observed during those treatments is the formation of an oxide scale at the surface which can play a protective role. However instabilities in the oxide formation have also been reported [30], and the exact nature of oxidation mechanisms on zirconium alloys remain to be solved.

2.3 Zirconia ceramics.

Until fifteen years ago, zirconia would not have been considered a candidate to be developed as an engineering ceramic because its polymorphism can lead to such large strains that it is self-fracturing. Research resulted in a new generation of zirconia-based materials prepared by sintering ultrafine powders prepared by special chemical processes. During sintering the zirconia formed is generally a monoclinic form, however

accompanied by a tetragonal form of unit cell volume 4-9% lower [30]. This sharp volume decrease subjects ZrO_2 artifacts to large strains and very large tensile stresses sufficient to break up a single crystal. To counteract the effect of the monoclinic-to-tetragonal transformation, alloying with a cubic oxide has been tried with aliovalent metal cations larger than Zr^{4+}; the materials obtained are known as partially stabilized zirconia, PSZ for short. Common additives that lead to these forms are MgO, CaO, and Y_2O_3 . Alloying with these elements accounts for significant gains in toughness and strength. Table 2.1 shows values of the Vickers hardness H_v and fracture toughness K_{1c} obtained by indentation methods.

Material	**Form**	**Hardness H_v (Gpa)**	**Toughness K_{1c} ($MPa.m^{1/2}$)**
Pure ZrO_2	monoclinic single crystal	6.5	1.1
ZrO_2-Y_2O_3 (PSZ)	tetragonal	11.7	6.9
ZrO_2-MgO (PSZ)	cubic	15.5	_

Table 2.1: Hardness and toughness data for zirconia and PSZ [30].

As lightweight materials with a low coefficient of friction, zirconia ceramics can be used for the bearing surfaces of joint implants. For hip replacement, femorals heads made of ceramic zirconia materials are widely used for their excellent tribological properties. [9]. There is indeed evidence that alumina (Al_2O_3) or zirconia (ZrO_2) ceramic bearing surfaces produce less friction and UHMWPE wear debris than metal bearing surfaces such as Co-Cr-Mo, and particularly Ti-6Al-4V (which are both commonly used for the articulating components of hip and knee prostheses) [11-13] . The hardness of those ceramic surfaces is particularly advantageous; however, the use of ceramics as a

material for the whole knee or hip implant is not widespread because of their poor toughness and impact resistance, especially in tension [8]. Hence, there is interest in a method of oxidation of Zr-2.5Nb alloys which can result in a modified zirconia surface with enhanced tribological properties while keeping the adequate bulk mechanical properties of the zirconium alloy.

2.4 Oxidation of zirconium alloys

Inward growth of the oxide.

Zirconium alloys oxidize by inward oxygen diffusion, as opposed to other materials like nickel alloys which oxidize principally by outward diffusion of cations [31]. In a first step, oxygen dissociates and dissolves into the alloy. A reaction follows between zirconium and oxygen which results in a protective zirconium oxide (ZrO_2) film, and later scale, on the surface. Oxygen diffuses readily through the scale, so new oxide is formed at the bottom of the scale, at the scale/substrate interface. Figure 2.4 depicts the principal stages of the oxide growth; the alloy/scale interface is expected to be irregular due to variable reaction kinetics with alloy grains of various orientation, whereas the surface of the scale is likely to remain unchanged and even. This inward oxygen diffusion is largely due to oxygen vacancies facilitating bulk diffusion and transport in the oxide, and columnar grain boundaries in the oxide promoting the transport of oxygen to the bottom of the scale [6,7]. Zr^{4+} ions are known to be very slow in diffusing in the oxide, especially compared to O^{2-} ions.

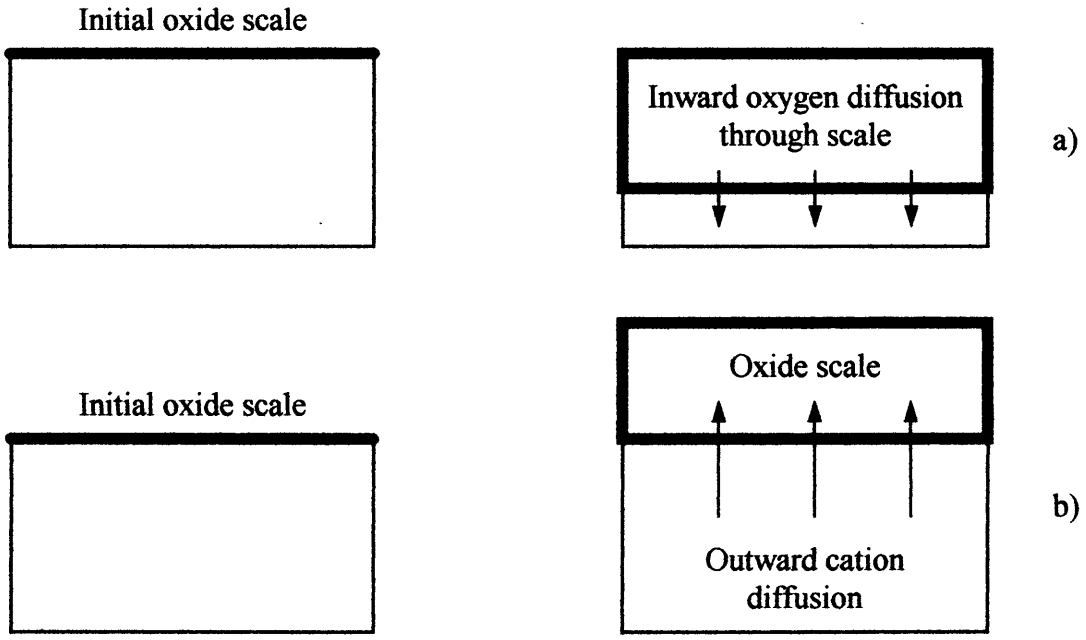

Figure 2.4: Schematic representation of oxidation steps
a) for inward growth.
b) for outward growth.

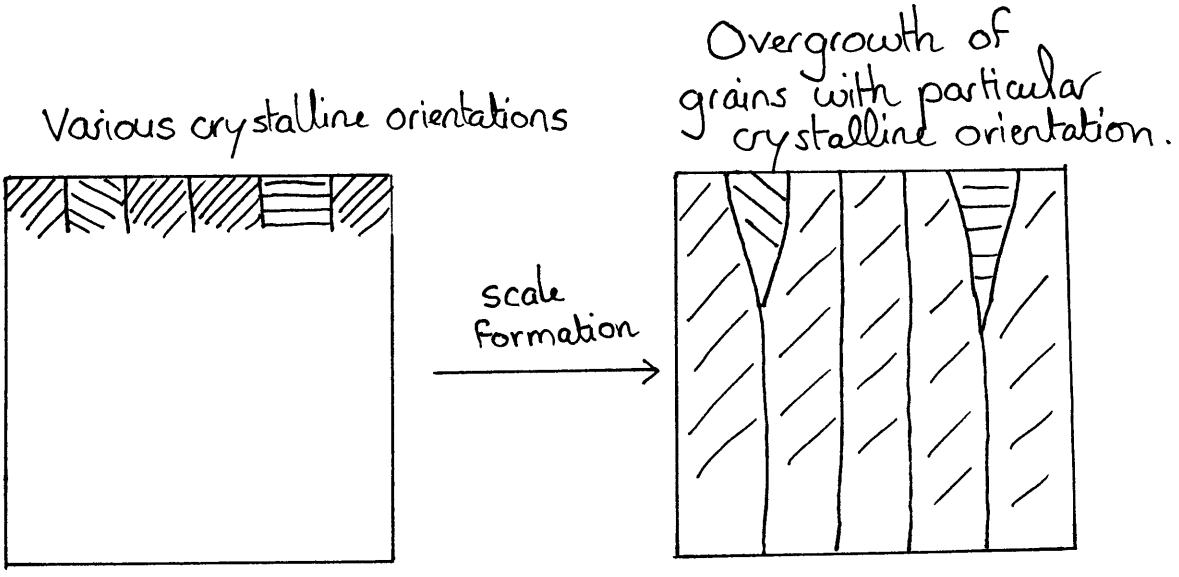

Figure 2.5: Schematic representation of oxide grain overgrowth.

Oxidation kinetics

The reaction kinetics are initially affected by the surface preparation of alloy, e.g. whether the alloy surface is abraded or chemically polished. The oxidation rate is also markedly dependent on differences in orientation between different grains. The oxidation kinetics also vary considerably with temperature [31]. Above 1000° C, the oxide growth follows parabolic oxidation kinetics: the oxide thickness is proportional to the square root of oxidation time. This indicates that oxidation is limited predominantly by solid state diffusion. Below 1000° C however, the kinetic behavior can be either parabolic or non-parabolic, e.g cubic or even quartic. One reason for the non-parabolic behavior may be that the zirconium major component oxidizes principally by inward oxygen diffusion through grain boundaries in the scale [26,27]. Also, oxygen diffusion might not be the only rate-determining process [31]. The electrical characteristics of ZrO_2 must be considered as well. The oxide is an ionic conductor in some conditions; accordingly, electron transport may be a rate-controlling factor. All in all, there is need for additional evidence to clarify the oxidation mechanisms involved in the non-parabolic oxide growth.

Two very different oxidization products were observed for different preparation conditions: one is a highly protective and dense oxide, termed black oxide; by contrast, a white surface oxide can form which is porous, and poorly protective. In orthopedic applications, it is certainly desirable to avoid formation of the latter [1,2]. White surface oxide is a result of a kinetics phenomenon known as break-away oxidation. Kofstad [31] proposes a model to explain break-away oxidation, the accelerated reaction rate which appears after the initial, protective oxide growth. This phenomenon can occur in water vapour or dry atmosphere. Impurities present in the metal appear to favor breakaway oxidation. By causing local stresses, their presence might contribute to the formation of precipitates and cracks in the alloy and the oxide which accelerate oxidation.

Microstructural transformations

Newcomb [22] has described the microstructure of a zircalloy-4 (Zr-1.50Sn-0.19Fe-0.10Cr-1280ppmO-30ppmH) oxidized at 500° C in pure oxygen for 28 hours.

Figure 2.6 shows the division of the oxidized area into several zones. The morphology of the oxide is columnar. In zone A (near the surface), the columnar grains are typically 300-500 nm in length and 10-30 nm in width. The diffraction patterns taken from the scale showed that the oxide is monoclinic m-ZrO_2, and exhibits texture. The formation of crystallographic texture in the oxide can be explained using kinetic considerations. Before oxidation begins, the alloy grains at the surface of the substrate possess various crystallographic orientations. As the protective oxide film starts forming at the zirconium alloy surface, the kinetics of ZrO_2 formation are favoured by some specific orientations. The oxide grains in these preferential orientations progress faster and deeper into the alloy, and undercut slower growing oxide grains; this is called grain overgrowth and is illustrated in figure 2.5. As expected, Newcomb [22] found that the oxide texture increases with depth, and is maximized in zone B (figure 2.6) of the oxide near the interface.

The interface (zone C), extending over depths of ~0.2 μm has a characteristic 'sawtooth' morphology so that the region consists of interlocking oxide and modified alloy grains beneath it. The zone D metal beneath the oxide was found to be both structurally and chemically modified over a depth of approximately 0.75 μm: it appears that recrystallization has occurred, and that lath-like structures have formed inside the alloy grains. These observations thus suggest structural transformations ocurring in a suboxide zone of the alloy prior to complete oxidation.

Lin [24] has described the microstructure of oxidized Zr-2.5wt%Nb alloy. The hexagonal-close-packed (hcp) α-Zr (containing ~1% Nb) can accomodate up to 26% oxygen in solid solution or as a suboxide, while the body-centered-cubic (bcc) β-Zr (containing ~20% Nb) phase, dissolving only ppm oxygen, is metastable and transforms eventually to the bcc β-Nb phase (containing ~80%Nb), sometimes with the appearance of intermediate ω-phase. The α-Zr component oxidizes to mostly columnar monoclinic (m-) ZrO_2 with 10-40 nm grain width, while the β-Zr sheath appears to oxidize to m-ZrO_2 as well, but with a much smaller grain size ostensibly determined by that of the intermediate ω-phase. The phase diagram of ZrO_2-Nb_2O_5 (figure 5.4, [33]) sums up the

possible phase equilibria occurring in the niobium-enriched grains. Microcracks or thin pores were noted at the interfaces between oxidized α-Zr and oxidized β-Zr regions [24]. Smaller amounts of tetragonal (t-) ZrO_2 have also been ostensibly detected, perhaps stabilized by the Nb content [27]. Oxidation of the β-Nb transformation product (as well as of the Nb-enriched β-Zr surrounding ω-phase) was observed to give rise to local regions in the oxide of higher Nb content, which appeared amorphous - with a composition close to Nb_2O_5 - in older (outer) regions of the scale; and as an incompletely oxidized crystalline suboxide of β-Nb in newer (inner) regions closer to the growth front [24]. Microfissures found adjacent to the Nb-rich amorphous oxide inclusions have been ascribed to the volume change in transformation from a suboxide to an amorphous oxide.

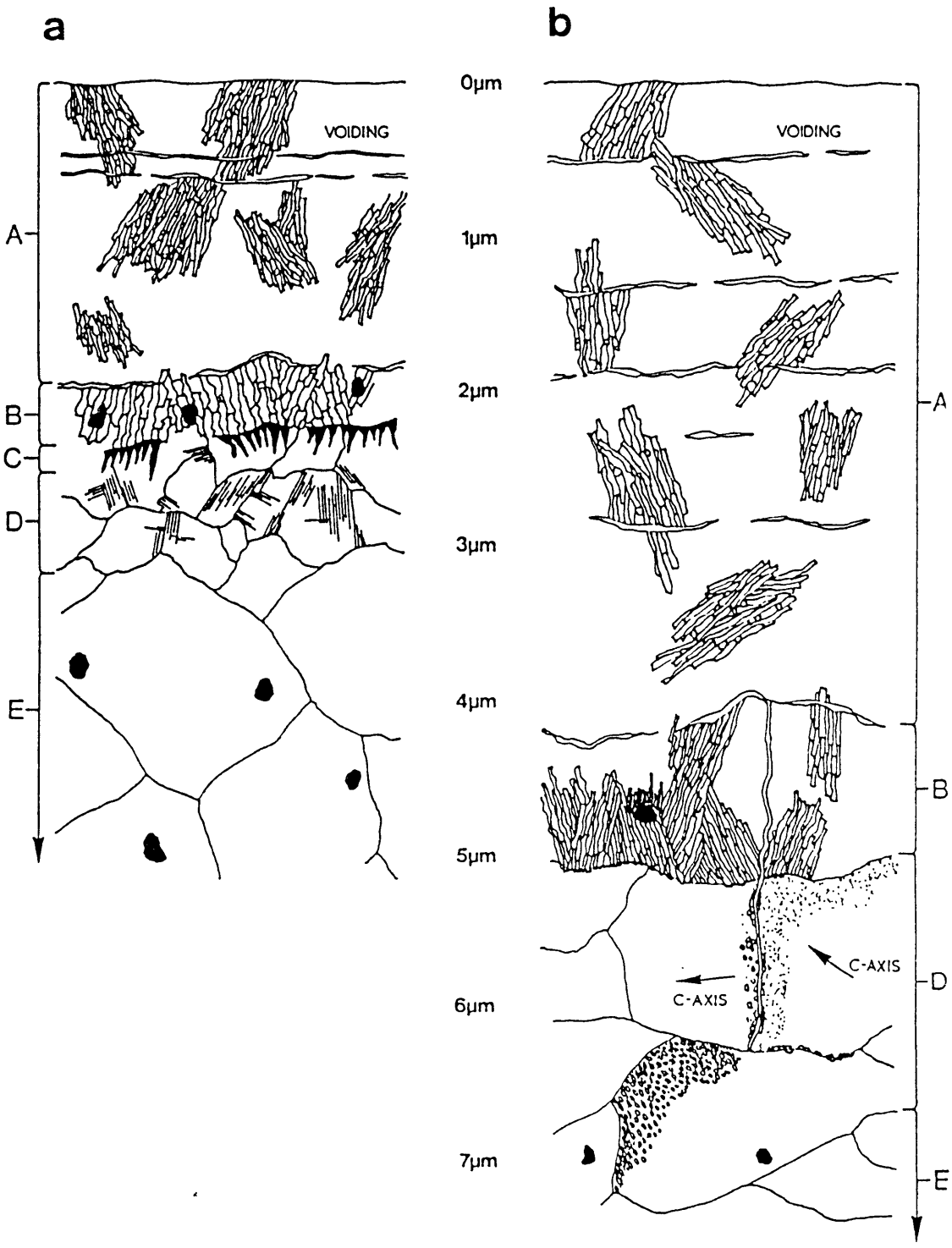

Figure 2.6: Schematic summary diagrams showing observed microstructures of the oxide and sub-scale for zircalloy-4 oxidation [22].

Chapter 3:

Experimental procedure

3.1 Kinetics

Thermogravimetric measurements were carried out in a Dupont Model 990 TGA microbalance unit incorporating a small-diameter furnace tube supplied with dry flowing air. The instrument is capable of measuring small weight gains while oxidation of the specimens occurs *in situ*. The specimens were coupons machined from barstock of Zr-2.5%Nb alloy supplied by Smith & Nephew, Inc., Orthopaedics Division. The faces of alloy coupons were polished to a 600-grit finish, washed in acetone and air-dried before oxidizing. The mass gain was plotted with oxidation time, and the oxidation reaction rate was evaluated by plotting the logarithm of the mass gain against logarithm of oxidation time. Coupons were oxidized at different temperatures: 600° C (1112° F), 635° C (1175° F), and 700° C (1292° F). Weight gain was measured for 6 hours. Coupons polished to a 1200-grit finish were also oxidized to study the influence of surface finish. Coupons of pure zirconium were similarly oxidized for comparison to the Zr-2.5%Nb alloy.

3.2 Alloy and preparation of wafers.

Specimens were prepared from 35mm (1.375 in) diameter wrought Zr-2.5Nb barstock material. The barstock was obtained from the Orthopaedics Division of Smith & Nephew, Inc. Wafers of 10 mm width were sawn from the barstock using a diamond wafering saw, as shown in figure 3.1. Before oxidation, a proprietary surface-finishing process was applied to the wafers. Various time and temperature combinations were explored in the oxidation, summarized in table 3.1 which shows the various time and temperature parameters. As a result of the wrought processing, the alloy microstructure was anisotropic. Two oxidation faces, transverse and longitudinal, were therefore distinguished and are defined in figure 3.1. For TEM cross-sections of the longitudinal face, square oxidized wafers (provided by Smith & Nephews, Inc.) were used instead of wafers sawn from the cylindrical barstock.

Temperature	Times
593° C(1100° F)	0.5 hour, 1 hour and 4 hours.
635° C (1175° F)	4 hours.

Table 3.1: Oxidation parameters.

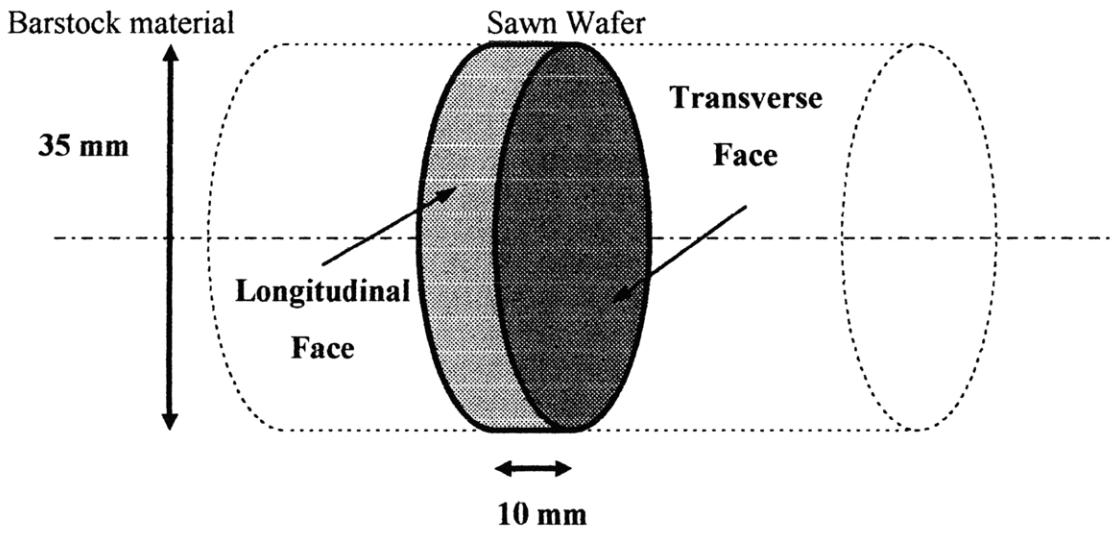

Figure 3.1: Schematic representation of barstock and sawn wafer, showing the transverse and longitudinal faces.

3.3 ESEM sample preparation.

Observations were made with an Electroscan ESEM. This microscope observes the sample in an atmosphere of typically 1-10 torr (~0.1-1 kPa) of water vapor. The best spatial resolution is about 7 nm. The specimen preparation for ESEM has the advantage of being minimal and allows a fast turn-around. The prepared samples were also examined by reflected light microscopy (RLM). Square coupons were sawn from the wafer. A thin (10nm) layer of gold was sputtered onto the oxide surface, followed by nickel plating (see section 3.3 for more detail on the procedure). The plated coupons were then mounted on a polishing platen and metallographically polished through 0.3 μm alumina grit to reveal the alloy substrate, oxide, and both interfaces in cross-section. The microscope is especially easy to operate, is fully digital, and is equipped with an X-ray analysis system for microanalysis system and elemental mapping.

The ESEM microscope is also invaluable for observing changes in samples during *in situ* oxide growth (a 1000° C hot stage is available), though no *in situ* observations of oxidation were made in this study, and for general purpose microscopy of scale surface morphology, for which no specimen preparation was required.

3.4 TEM Specimen Preparation.

a) Slicing.

Using a Buehler diamond wafering blade, bars 30-mm long with a rectangular section 2mm x 1mm were sliced out of the oxidized wafers. Figure 3.2 shows how these bars were sliced so that one side only has an oxide surface. The figure also shows that, for cross-sections on the longitudinal face, oxidized square wafers were used instead of cylindrical ones.

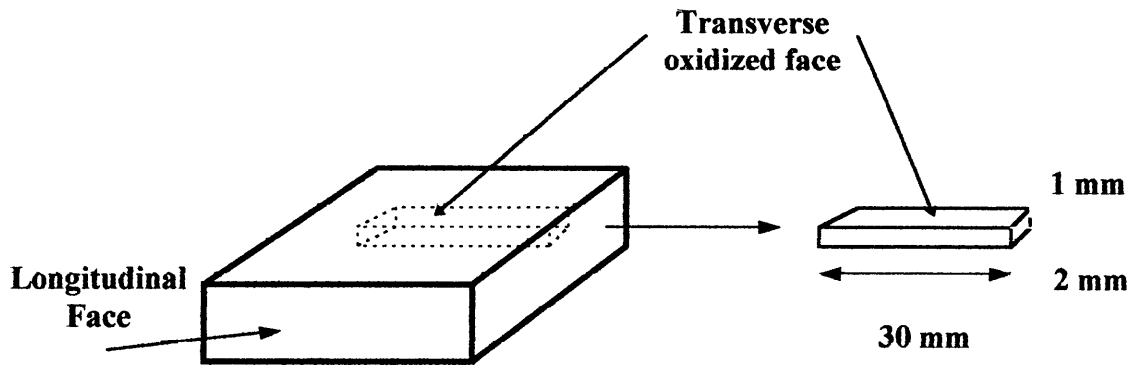

Figure 3.2: Schematic representation of the procedure for slicing a wafer into a bar for TEM transverse cross-sections.

b) Nickel plating.

Nickel plating is an electrochemical process which was chosen because it is a very efficient way to encase the bar in a nickel metal layer to prevent the composite oxide/alloy sample from falling apart during the successive stages of specimen thinning. The edges of the bar were rounded to avoid sharp angles difficult to nickel plate. A platinum wire was wound into a notch at the top of the bar. The oxidized face was coated with 10 nm sputtered pure gold, in order to provide a conducting surface for the nickel plating. Figure 3.3 shows the experimental apparatus for nickel plating. A standard (Watt's bath) solution saturated with nickel sulfate was used as electrolyte. A rectangular pure nickel anode and the bar were kept immersed facing each other 1 cm apart (with no direct contact) in the solution at a controlled temperature of 50° C. A DC source induced a plating current density of 10 mA/cm^2. Once the rod was coated with a nickel layer close to 1 mm thick, which could take up to 70 hours, the rod was removed from the bath and rinsed with deionized water.

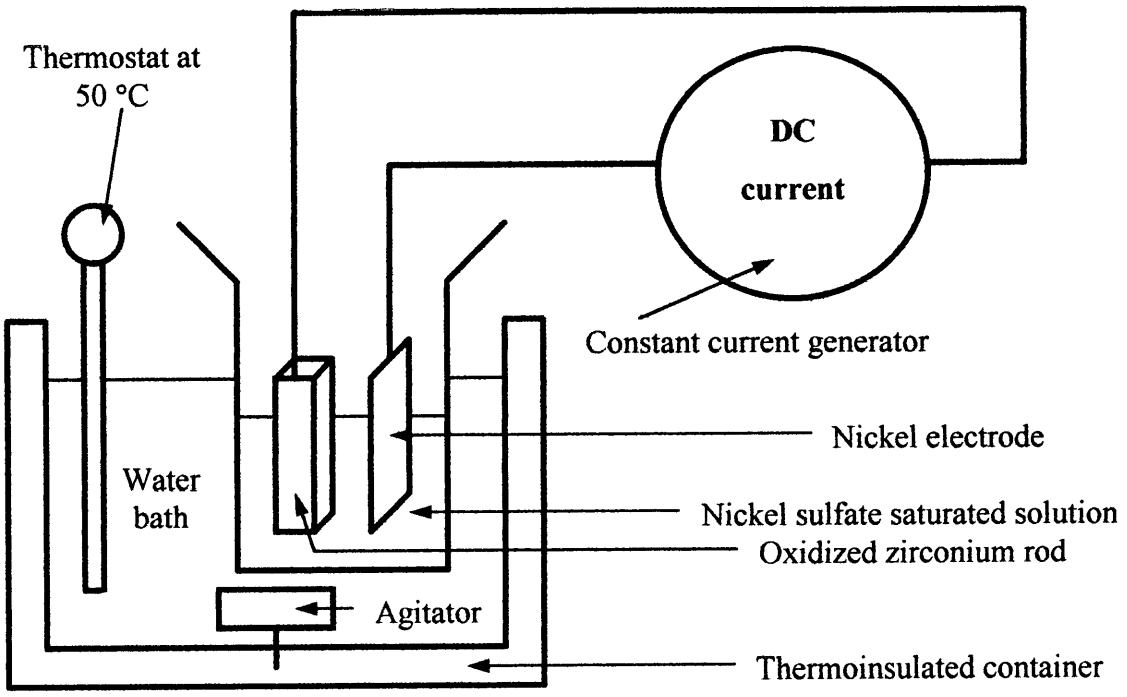

Figure 3.3: Schematic representation of the apparatus for nickel plating.

c) Polishing.

The plated bar was then sectioned into slices between 250 and 400 μm thick with the Buehler diamond wafering blade. One slice was selected and mounted on a glass disk of ~1 cm diameter with crystal bond. Before mounting, it was ascertained that the thickness of the slice was uniform to within 1 μm. Using a Minimet polishing machine, one side of the mounted slice was polished to a 1 μm finish, using increasingly finer polishing media: metal plates embedded with 30 and 15 μm diamond particles, then diamond pastes for 6, 3, finally 1 μm finish. The glass plate was then heated to melt the crystal bond, and the slice was inverted and remounted. This time, a minimum amount of crystal bond was used for mounting to ensure that the two polished surfaces remained parallel. The final specimen thickness was reduced to between 90 and 120 μm, with a 1 μm finish on both sides.

d) Dimpling.

Final mechanical thinning was achieved with a dimpler. The dimpler was used to reduce the thickness locally to 10 μm with 100 μm thick periphery for added specimen support (see figure 3.4). This configuration greatly facilitates handling of thin or brittle materials. The concept of a dimpler is simple; the specimen is mounted on a specimen table (platen) which rotates on a vertical axis, while the grinding tool, mounted on a precision spindle attached to a viscously damped pivot arm, rotates on an orthogonal, horizontal axis (figure 3.4). The working pressure of the arm can be adjusted to produce the desired removal rate by varying the force on the arm and, hence, on the grinding tool. Diamond polishing paste was added on the surface of the grinding tool to preclude work hardening and create a specular finish. The thickness of the section was accurately checked before dimpling, and the specimen mounted on the platen of the dimpling machine. Two precautions were taken: a minimum amount of crystal bond was applied, and the specimen was carefully positioned. An excess of crystal bond may prevent the sample from lying flat and will be difficult to remove after dimpling. The area of interest must be centered with respect to the cutting tool, so that in the end it actually lies at the thinnest of the prepared section. The section was first dimpled to 20 μm thickness at the thinnest point using 3 μm diamond paste, then further dimpled to 10 μm thickness or less with 1 μm paste.

e) Copper grid

After dimpling, a 3 mm diameter copper grid was attached to the thinned disk for additional support and protection of the outer edge. With the specimen still attached on the dimpler platen, the grid was glued on the surface with a minimum amount of quick drying epoxy. The grid had an oval hole which was aligned with the visible oxide band at the centre of the disk. Figure 3.5 depicts the surface of the specimen before and after gluing the grid.

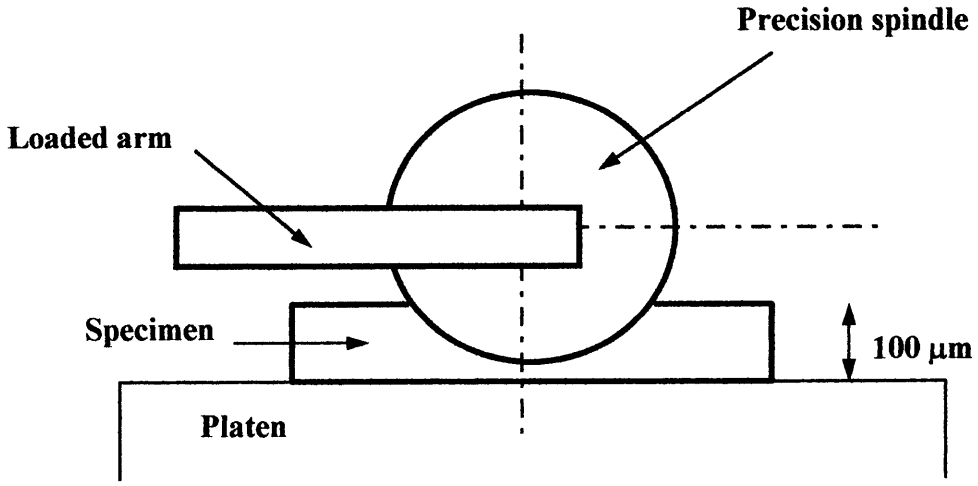

Figure 3.4: Schematic representation of the dimpler and specimen in the following configuration: dimpling is completed, specimen is still mounted on the dimpler platen, and the grinding spindle attached to the arm is not yet lifted.

f) Ion-milling.

The specimen was released from the platen by heating and melting the crystal bond. It was then mounted in the cold stage of a Gatan dual ion-mill. The cold stage prevented any heating of the specimen during ion-milling that might cause microstructural change or epoxy degradation. The principle of the ion-mill is to remove material very gradually by sputtering using two incident argon ion beams until the center of the specimen is transparent to a laser monitor. Ion-milling was carried out double-sided with the specimen rotating. The milling angle chosen was 15°. Figure 3.6 summarizes the principal stages of specimen thinning.

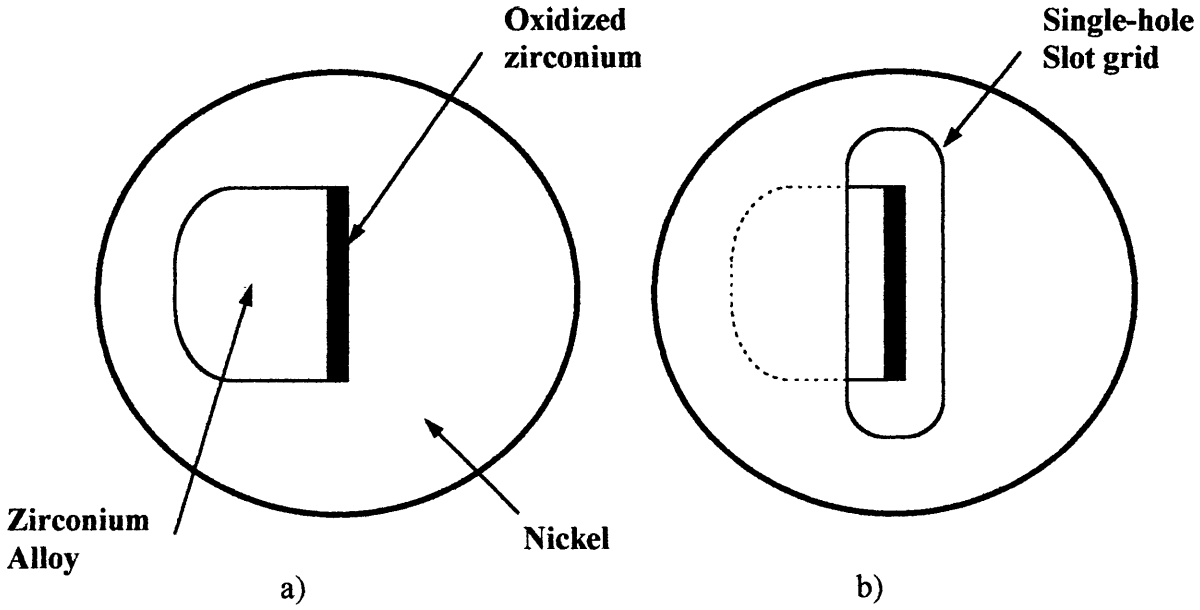

Figure 3.5: Schematic diagram showing the surface of the TEM sample a) before, and b) after, attaching the grid.

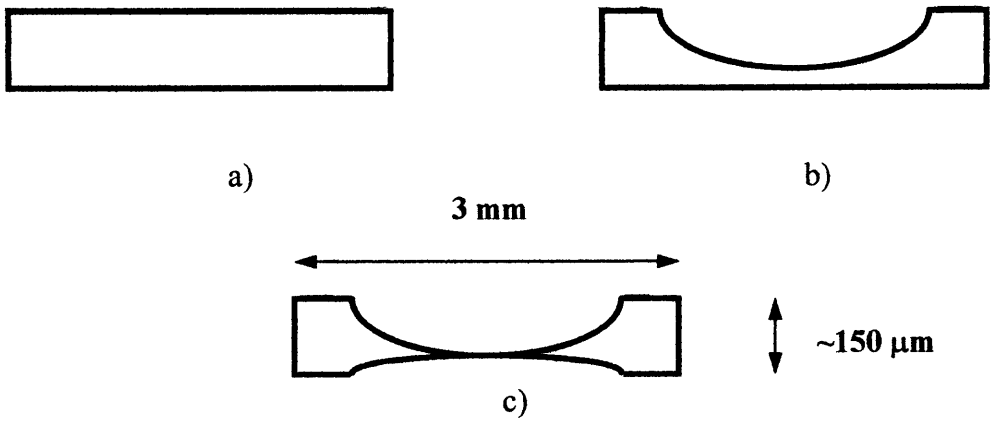

Figure 3.6: Schematic diagram showing the specimen section at different thinning stages:

a) Before dimpling

b) After dimpling

c) After ion-milling

3.5 TEM Observation.

a) Instrumentation.

Oxide microstructures were revealed by cross-section transmission electron microscopy (TEM). Two TEM machines were used: a JEOL 200 CX, and a JEOL 2000 FX. It was not found necessary to coat the thinned specimens with evaporated carbon, there being sufficient conductivity in the zirconia to preclude charging in the electron beam. The JEOL 200CX was operated at 200 kilovolts with a simple tungsten hairpin filament thermoionic emitter. The JEOL 2000 FX was operated at 200 kilovolts with a lanthanum hexaboride cathode. The latter instrument is capable of an ultimate point-to-point resolution of 0.28 nm, with the ability to image lattice fringes at 0.20 nm resolution. The pole piece allows for 35° of tilt in both directions.

b) Principle of transmission electron microscopy (TEM).

Microscopy is based on the ability to retrieve spatial information about an object, usually in magnified form, from diffraction or radiation by the object. The main concept of TEM is to use an electron beam passing through a thin (electron transparent) section of a specimen to visualize its transmission function. The information about the internal structure of the object is therefore averaged over its thickness, providing a two-dimensional mapping of features such as grain arrangements or structural defects. Figure 3.7 shows the configuration of a conventional transmission electron microscope (CTEM) and its optical analogue. The condenser, objective, and projector lenses of the CTEM function on electromagnetic principles. Together, they provide an overall magnification from 100 to 1 million times.

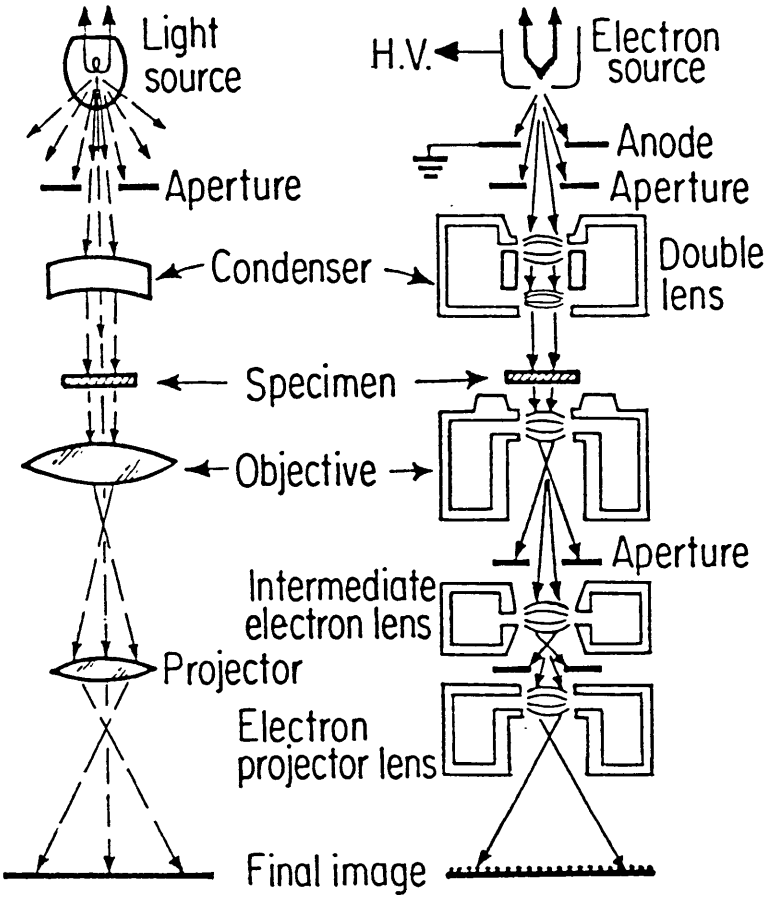

Figure 3.7: Schematic diagram showing the configuration of the conventional TEM and the optical analogue.

c) Operation of the electron microscope.

A liquid nitrogen cold finger was used to reduce hydrocarbon contamination in the vicinity of the specimen. The sample holder was positioned in the microscope at low magnification until the electron-transparent area was found. The electron beam issuing from the gun can be accelerated under a wide range of voltage from 40 to 200 kV (kilovolts). Although higher voltage brings a brighter image, greater penetration of the specimen, and higher resolution, energetic electrons can also induce knock-on radiation damage to the specimen. This was found not to be the case with zirconium or zirconium oxide, so the highest accelerating voltage was chosen. The observation time however, was limited to roughly 2 hours in any one area because of radiolysis of hydrocarbon molecules adsorbing onto the specimen surface. Standard microscope alignment procedures were followed. A selective area aperture was employed in diffraction mode, for which a camera length of typically 60 cm was chosen; the objective aperture was then centered on the optic axis at the diffraction plane. A small (10 μm) objective aperture was used in bright-field and dark-field diffraction contrast. Images were recorded on photographic plates.

d) Imaging techniques.

Diffraction patterns.

Electrons are diffracted from atoms or collections of atoms, and the distribution of diffracted electrons forms the diffraction pattern which, for the small (<1°) diffraction angles for 200 kV electrons, can be collected on a flat plate collector (the observation screen or photographic plate). TEM makes possible the further formation of an image of the area diffracting, which can be manipulated according to what portion of the diffraction pattern is allowed to contribute to that image. For a crystalline sample, the diffraction pattern consists of a set of discrete beams representing the intersection of the Ewald sphere with the reciprocal lattice of the crystal. These diffracted (Bragg) beams represent spatial periodicities in the sample. Figure 3.8 shows the Ewald construction in

the reciprocal space, which is convenient to explain how to retrieve the spatial information from the diffraction image. The Ewald construction consists of a sphere intersecting the origin (forward scattered beam) of the diffraction pattern, and whose radius of curvature is the wave number of the electron beam. For fast electrons, $\lambda \sim$ 1-4 pm, the radius of curvature of the Ewald sphere is very large compared to the reciprocal lattice point spacings; the Ewald sphere is therefore very flat, in fact almost planar. The reciprocal lattice points are in actuality spikes normal to the specimen plane whose length is inversely proportional to the specimen thickness. Since what is seen in the diffraction plane is actually the intersection of the Ewald sphere with the reciprocal lattice points, a consequence is the possibility to see many reciprocal lattice points represented in one diffraction pattern at the diffraction plane.

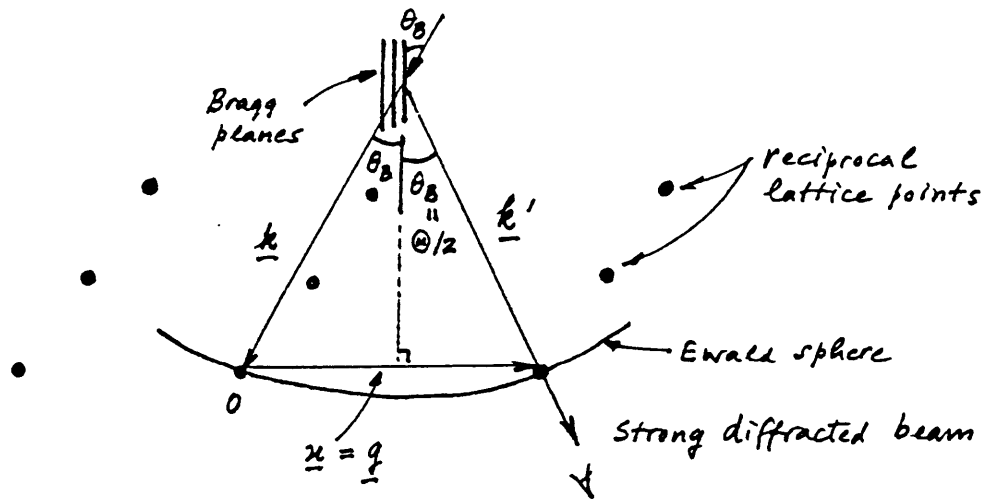

Figure 3.8: Ewald sphere construction for depicting sampling of reciprocal space.

Bright-field single beam imaging technique.

This technique has the advantage of being a fast and easy way to obtain a diffraction contrast image of the sample. It consists merely in centering the objective aperture, so that only the central forward scattered beam is selected, from which spatial information is retrieved (figure 3.9). However, a lot of information is lost by selecting this beam only (for example, information about periodicities), and the exact nature of the specimen information contributing to the contrast can be difficult to establish and to distinguish from imaging artefacts. A crystalline specimen is usually oriented close to the Bragg condition (two strong diffracted beams) to achieve maximum image brightness and contrast. Contrast occurs from orientational (strain) or scattering (structure factor) variations in the specimen.

Dark-field single-beam imaging technique.

With the dark-field technique, a region of reciprocal space away from the origin (for example, for a crystalline specimen, a single diffracted beam) is selected by the objective aperture. This has the advantage of retrieving more selective information, although the image brightness is usually greatly reduced (unless a crystalline specimen is oriented at the exact Bragg angle for the diffracted beam chosen). In switching from the bright-field mode to the dark-field mode, one tilts the incident beam to bring the diffracted beam to the optic axis to minimize astigmatism. This latter procedure shifts the whole diffraction pattern, but also rocks the Ewald sphere (figure 3.9), so that the specimen has to be tilted subsequently to achieve the same diffraction conditions, for example to obtain a diffraction pattern with two strong beams only. There is a compromise between strain sensitivity and image brightness. High strain sensitivity, and correspondingly narrow image of strain-producing features such as dislocations, can be achieved by orienting the specimen far from the Bragg condition, the so-called dark-field weak-beam method. The weak-beam method is ideal for detecting microstructural defects whose contrast is otherwise drowned in other contrast features in the strong-beam bright-field mode.

Imaging with two or more beams.

Selecting two beams (figure 3.9) can result in periodic contrast, from the interference of the two beams, corresponding approximately to the spacing of lattice planes in a crystalline specimen, provided there is sufficient spatial resolution in the microscope. The conditions under which such high resolution images coincide with actual projected atomic features are strictly circumscribed and are beyond the scope of this thesis. Multibeam imaging was not employed in the present investigation, since the cross-sections were seldom sufficiently thin to render this high-resolution imaging mode practicable.

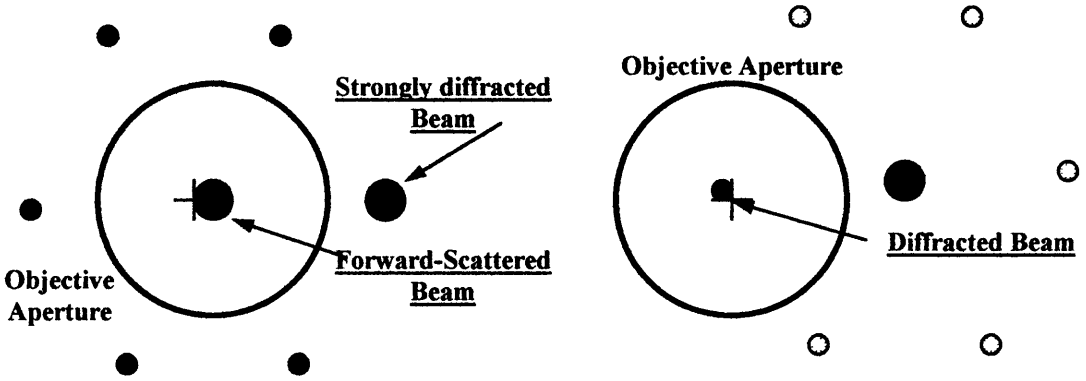

a)
Strong-beam bright-field imaging,

b)
Weak-beam dark-field imaging,

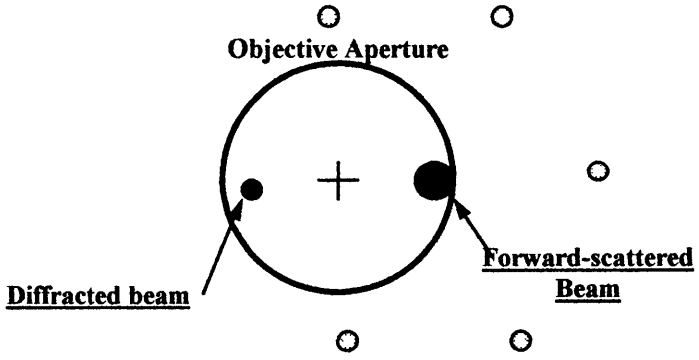

c)
Two-beam imaging

Figure 3.9: Imaging conditions at the diffraction plane, showing placement of objective aperture (circle) and optic axis (+).

3.6 STEM Observation.

a) STEM imaging.

In conventional TEM, the entire area is illuminated at once, and the information about each point in the object is therefore acquired in *parallel*. In STEM, the image is acquired *serially*, since each point of the area of interest is scanned separately. Figure 3.10 shows the equivalence of conventional TEM and STEM in image collection. The STEM is configured with a condenser system used to focus the electron beam to a fine spot as small as 0.5 nm diameter on the specimen object. This fine probe is scanned over the specimen, by means of scanning coils, in synchronization with an electron beam in a cathode ray tube whose intensity is modulated by a detector collecting electrons transmitted through the specimen. The resolution is set by the probe diameter and its spreading by diffraction processes in the specimen. In this study, a VG HB603 scanning transmission electron microscope, an advanced analytical electron microscope operating at 250 kV, was used. It has a field-emission electron gun, and a large-angle windowless X-ray detector. This STEM has a 0.5 nm electron probe and includes an unusual range of diffracting and imaging capabilities.

b) STEM Compositional analysis.

X-rays generated by the electron probe can be analyzed at each point scanned by the probe (by energy dispersion in a Li-drifted Si detector), and X-ray image maps can be acquired (by using the X-ray detector output to modulate the image display) to provide information about elemental spatial distribution. Microanalysis in STEM can be carried out on an exquisitely fine scale, and is capable for example of detecting a monolayer of foreign atoms segregated to an interface. The associated computer system can generate elemental maps of samples, illustrating the distribution of elements. STEM was used to map the presence of niobium in the Zr-2.5Nb alloy and in the oxide subsequently formed, using the technique of energy-dispersive X-ray analysis (XEDS). An elemental composition analysis was conducted simultaneously with image acquisition to assess the niobium content in the zones appearing enriched in that element. Oxygen presence was also mapped to determine clearly were the interface between the oxide and the metal lay.

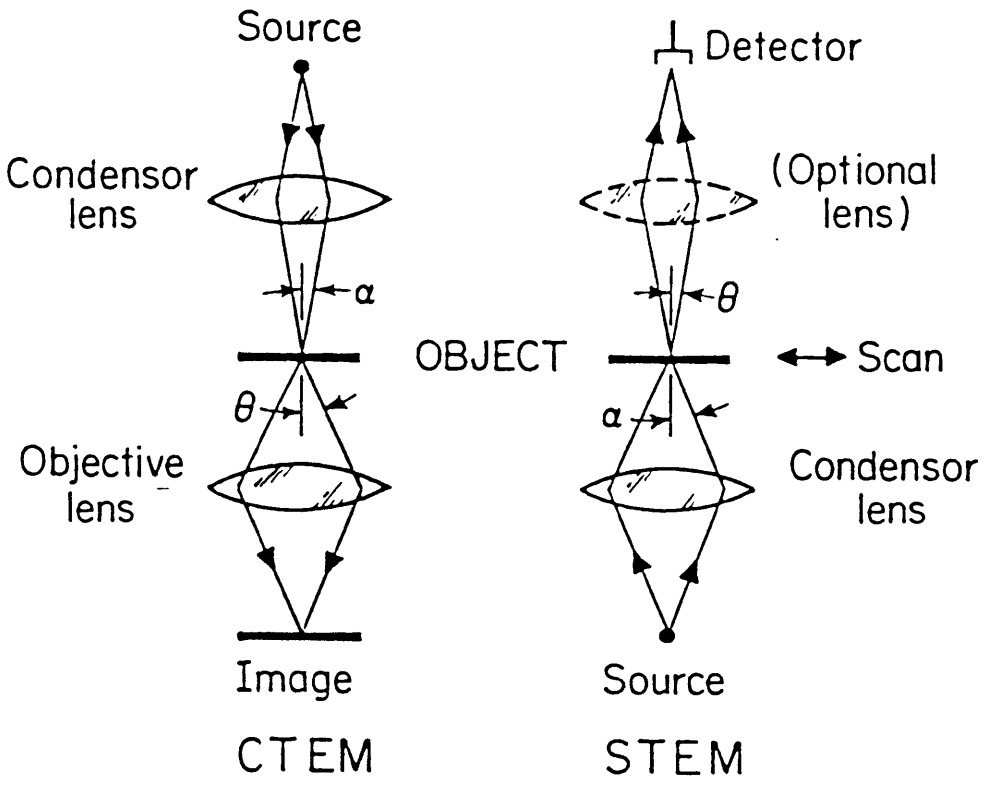

Figure 3.10: Schematic diagram showing the equivalence between
a) a conventional TEM and,
b) a STEM.

Chapter 4:

Experimental Results

4.1 Kinetics

Oxidation rates and behaviour.

Figure 4.1 [25] shows a typical mass gain curve for a 6-hr oxidation experiment in dry air at 600° C (1112° F) obtained by thermogravimetric measurements in the TGA microbalance. The oxidation experiment was conducted on Zr-2.5%Nb alloy coupons polished to a 600-grit finish. A log-log plot of the data (figure 4.2, [25]) reveals that the kinetics are considerably faster than parabolic for the first 40 minutes and approach parabolic behaviour for times greater than 100 minutes. Indeed, for the first 40 minutes of oxidation, the kinetic exponent is m=1.02, very close to linear kinetics. After 100 minutes, the kinetic exponent m=0.54 is very close to parabolic (m=0.50). The values of m between 40 and 100 minutes gradually decrease from 1.02 to 0.54.

Oxidation on the transverse and longitudinal faces of the substrate

Figure 4.3 [25] shows the weight gain curves and the parabolic kinetic plots for the oxidation of the Zr-2.5wt.%Nb substrate at 600° C and 700° C (1192° F) for 6 hours in dry air on transverse and longitudinal faces. The oxide appears to have grown approximately 10% faster on the transverse (TD) face than on the longitudinal (RD) face at 600° C. Figure 4.4 [25] shows the same curves obtained this time for oxidation at 635° C (1175° F) for 6 hours. A 10% difference in the reaction rates appears as well between the oxidation on the transverse and longitudinal faces, although the largest rate difference between the faces appears in the earliest stages of oxidation. Comparing the results between figures 4.3 and 4.4 [25], the oxidation rate is about 30% higher at 635° C than at 600° C. At 700° C (figure 4.3b, [25]), it is about twice as high as at 635° C.

Substrate preparation and niobium content.

It was found that coupons polished to a 1200-grit finish oxidized 30% less quickly in the initial stage, but oxidized only about 5% more slowly after 3 hours; it appears that the influence of the substrate surface finish is stronger during the earliest stages of oxidation. The oxidation rate of the Zr-2.5%wtNb substrate was also compared to that of pure zirconium; figure 4.4 [25] shows that the oxidation rate for pure Zr at 635° C is about half that of the alloy.

4.2 ESEM Results.

ESEM was used to examine the surface morphology of the oxide. Figure 4.5a [25] shows ESEM micrographs normal to the oxide surface formed on Zr-2.5wt%Nb oxidized in the X-ray hot-stage at 600° C for 6 hours in air. They reveal parallel cracks spaced 50-70 μm apart, and linked by smaller cracks. The straight lines randomly distributed and oriented are scratches resulting from metallographic polishing of the surface. These lines do not run as deep inside the scale as the cracks, therefore reflect more light and have a different nature. An enlargement (figure 4.5b, [25]) shows an example of a linking crack. The same oxidation conditions (600° C for 6 hours in air) in a TGA microbalance were used to prepare samples for observations of cross sections through the oxide scale with ESEM and reflected light microscopy (RLM). The RLM micrographs reveal a largely intact oxide which varies from 2-4 μm in thickness (the sputtered gold and the plated nickel can be seen at the top of the oxide); minor cracking is observed roughly parallel to the interface in mid-scale. The ESEM metallographically polished cross section (figure 4.6, [25]) shows in order, top to bottom, nickel-plating, gold layer, oxide and substrate. It reveals a fairly flat oxide surface beneath the sputtered gold layer, and a wavy interface with the alloy substrate.

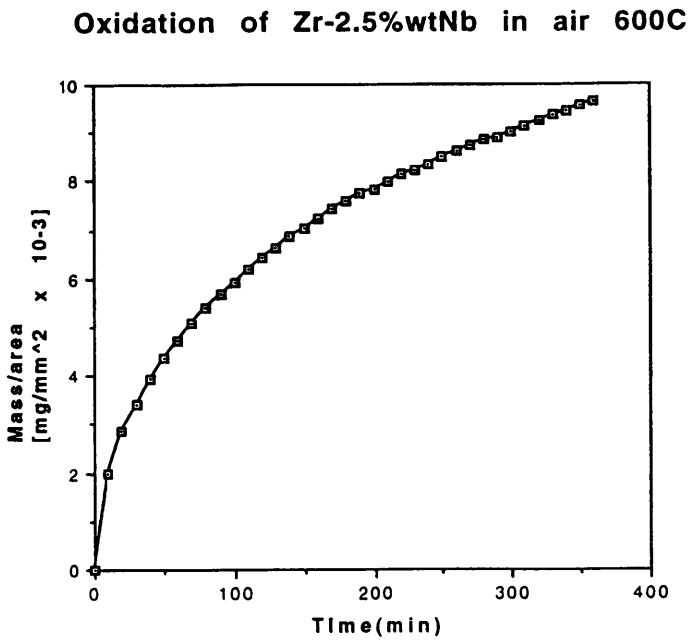

Figure 4.1: Weight gain kinetics for Zr-2.5wt%Nb oxidized 6h in dry air at 600° C [25].

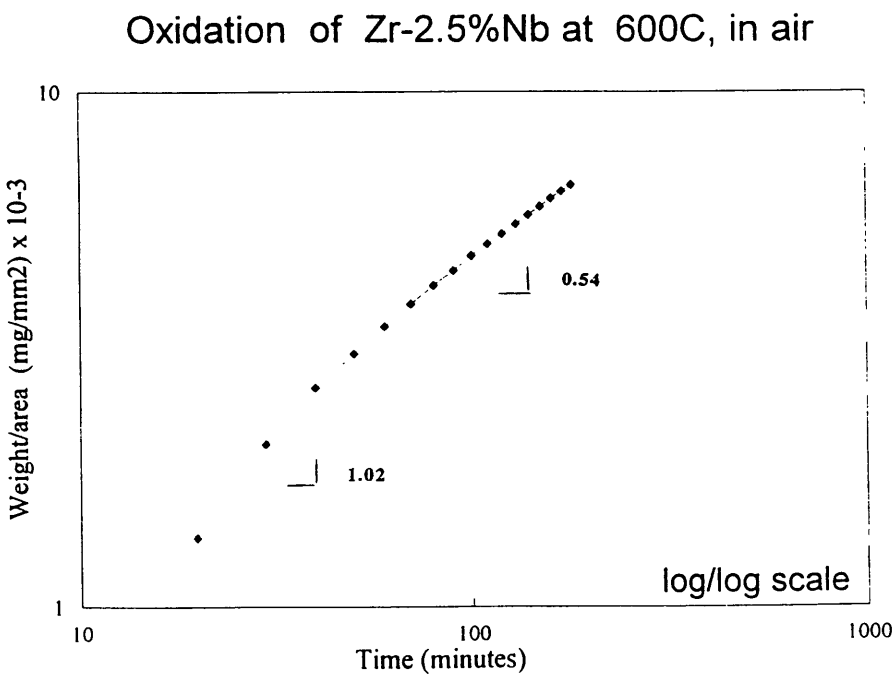

Figure 4.2: Log-log plot of oxidation kinetics in figure 4.1 [25].

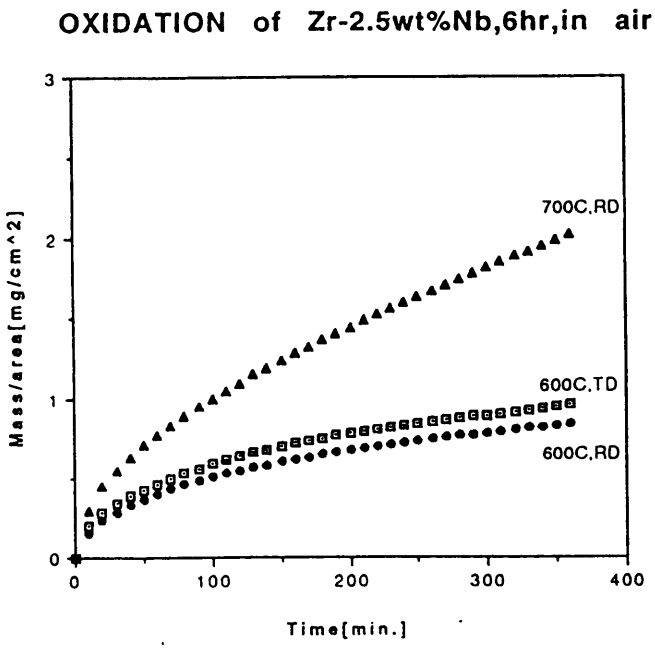

Figure 4.3: a) Weight gain kinetic plots for oxidized Zr-2.5wt%Nb at 600° C and 700° C in dry air on transverse and longitudinal faces [25].

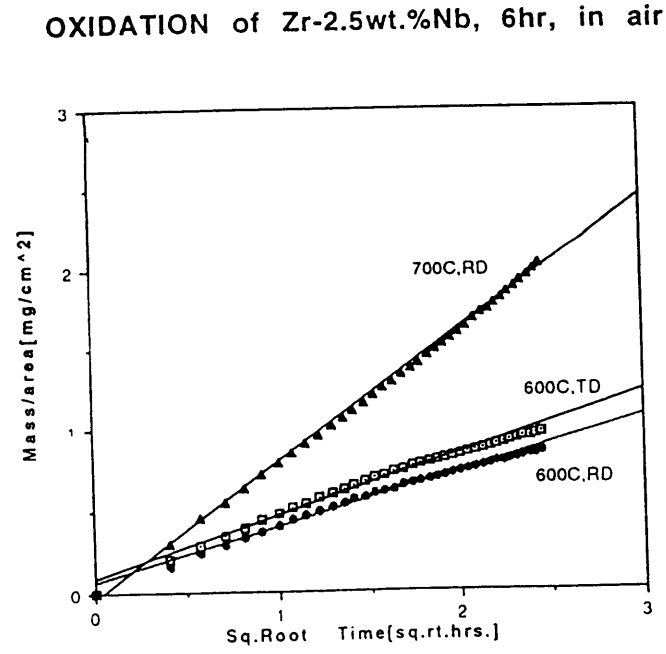

Figure 4.3: b) parabolic kinetic plots of a) [25].

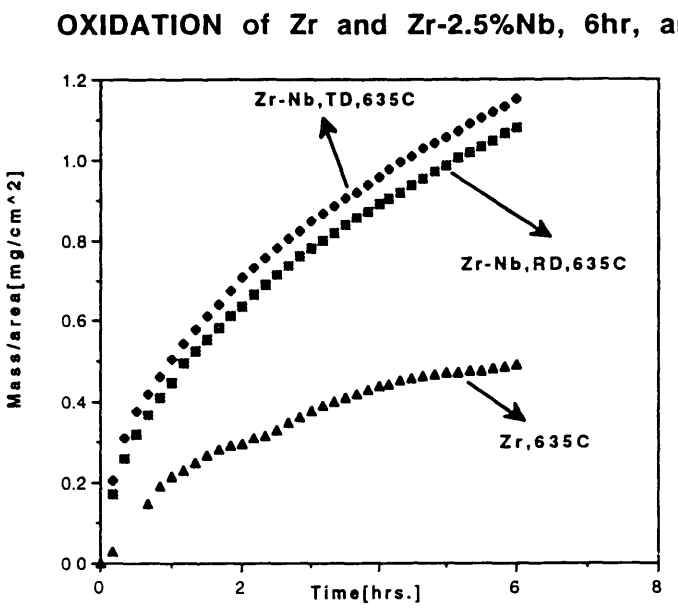

Figure 4.4: a) Weight gain kinetic plots for oxidized Zr-2.5wt%Nb at 635° C for 6 hours in dry air on transverse and longitudinal faces, compared to oxidation of pure zirconium [25].

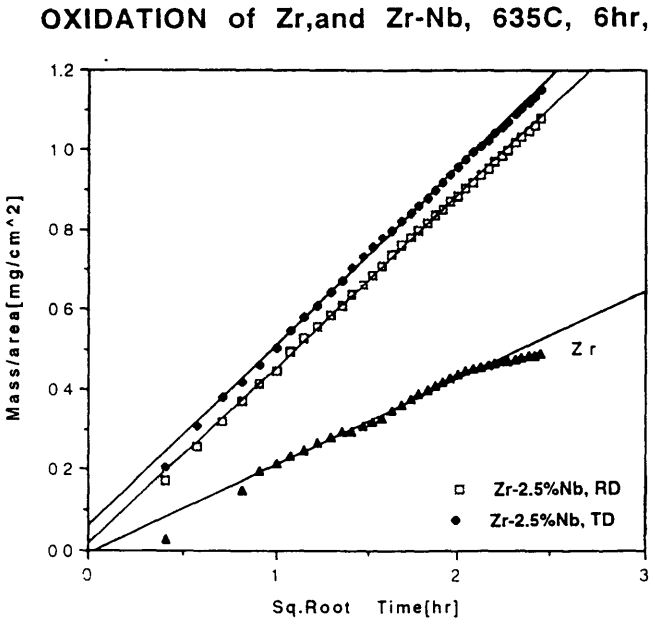

Figure 4.4: b) parabolic kinetic plots of a).

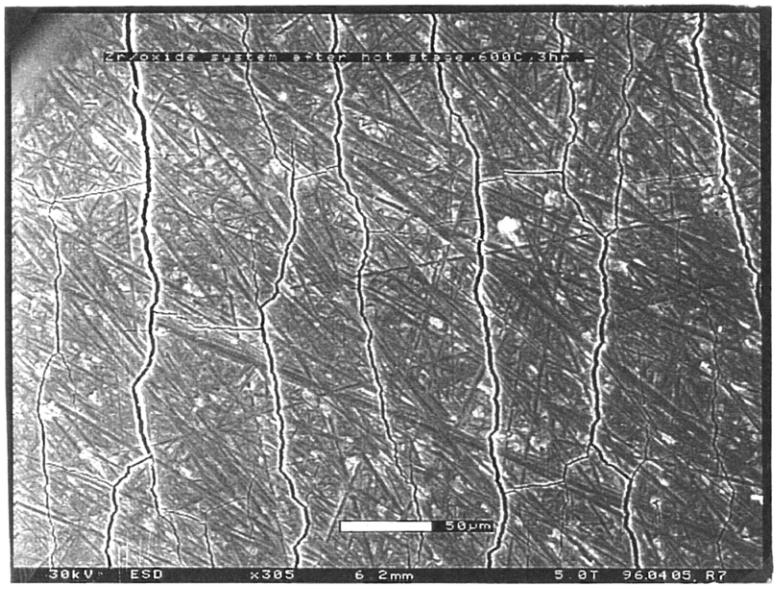

Figure 4.5: a) ESEM micrograph normal to oxide surface formed on Zr-2.5wt%Nb oxidized in the X-Ray hot-stage at 600° C for 6 hours in air.

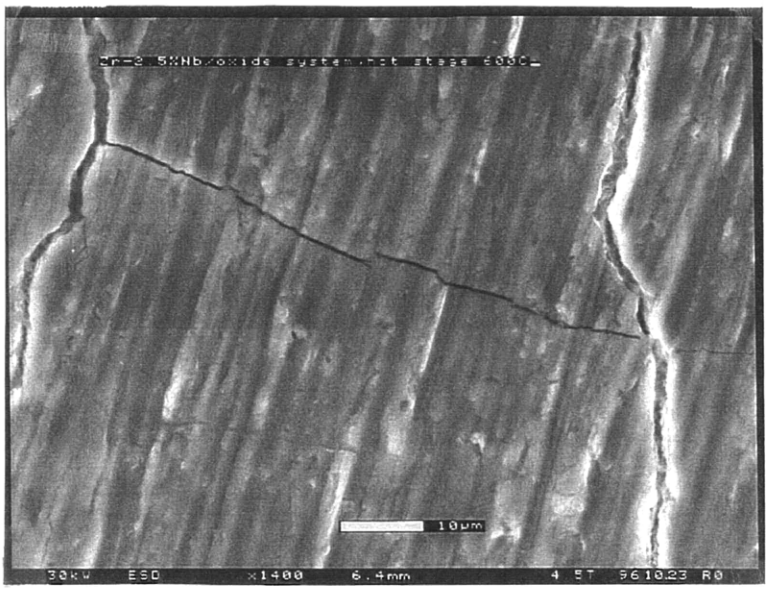

Figure 4.5: b) Enlargement of a).

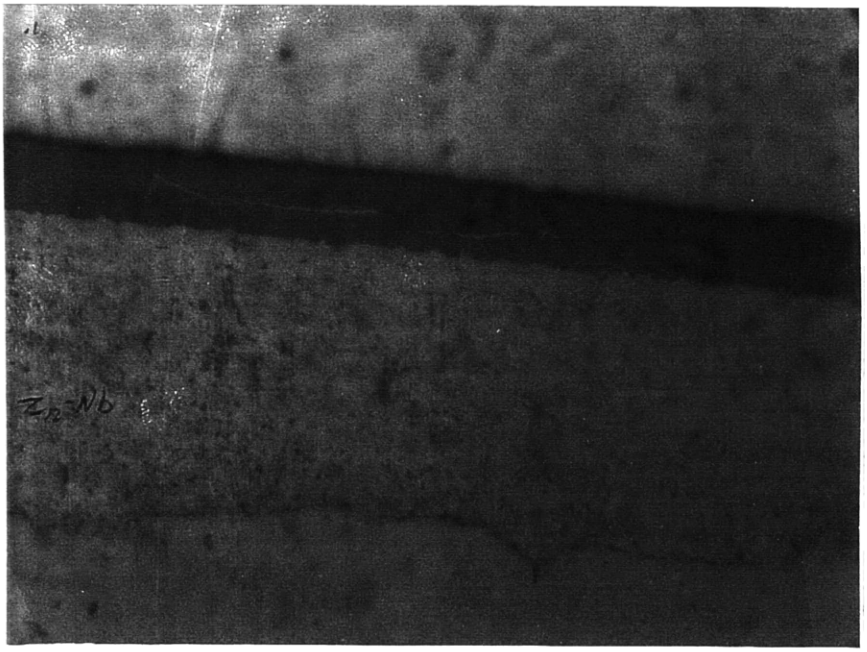

Figure 4.6: a) Reflected light micrograph of polished cross-section across oxide on Zr-2.5wt%Nb substrate oxidized 3 hours in the hot-stage, in air, at 600° C.

Figure 4.6: b) ESEM micrograph after oxidation in dry air in TGA at 600° C for 6 hours.

4.3 Microstructure of the Oxide and Interface

4.3.1 TEM Results.

Columnar structure.

Figure 4.7 [25] shows that under oxidation conditions below the alloy eutectoid, the oxide grows with a columnar microstructure directly from the alloy substrate. The micrograph is a dark-field image using a region of reciprocal space containing oxide diffraction rings. Figure 4.8 shows a bright-field image of the columnar structure on the transverse face of a specimen oxidized for 3 hours at 1100° F (593° C). The oxide is characterized by lath-like grains of monoclinic m-ZrO_2 oriented with their long axes normal to the interface between the oxide and the alloy, forming a columnar microstructure. The width of the grains varies between 40 and 75 nm. Several of these grains are highlighted in a dark-field micrograph (figure 4.9), in which the grains are in strong dynamical contrast. Moire fringe contrast is evident, due to overlapping of grains. These Moire fringes suggest a high degree of texture (approximately same crystal orientation) in the oxide grain orientations.

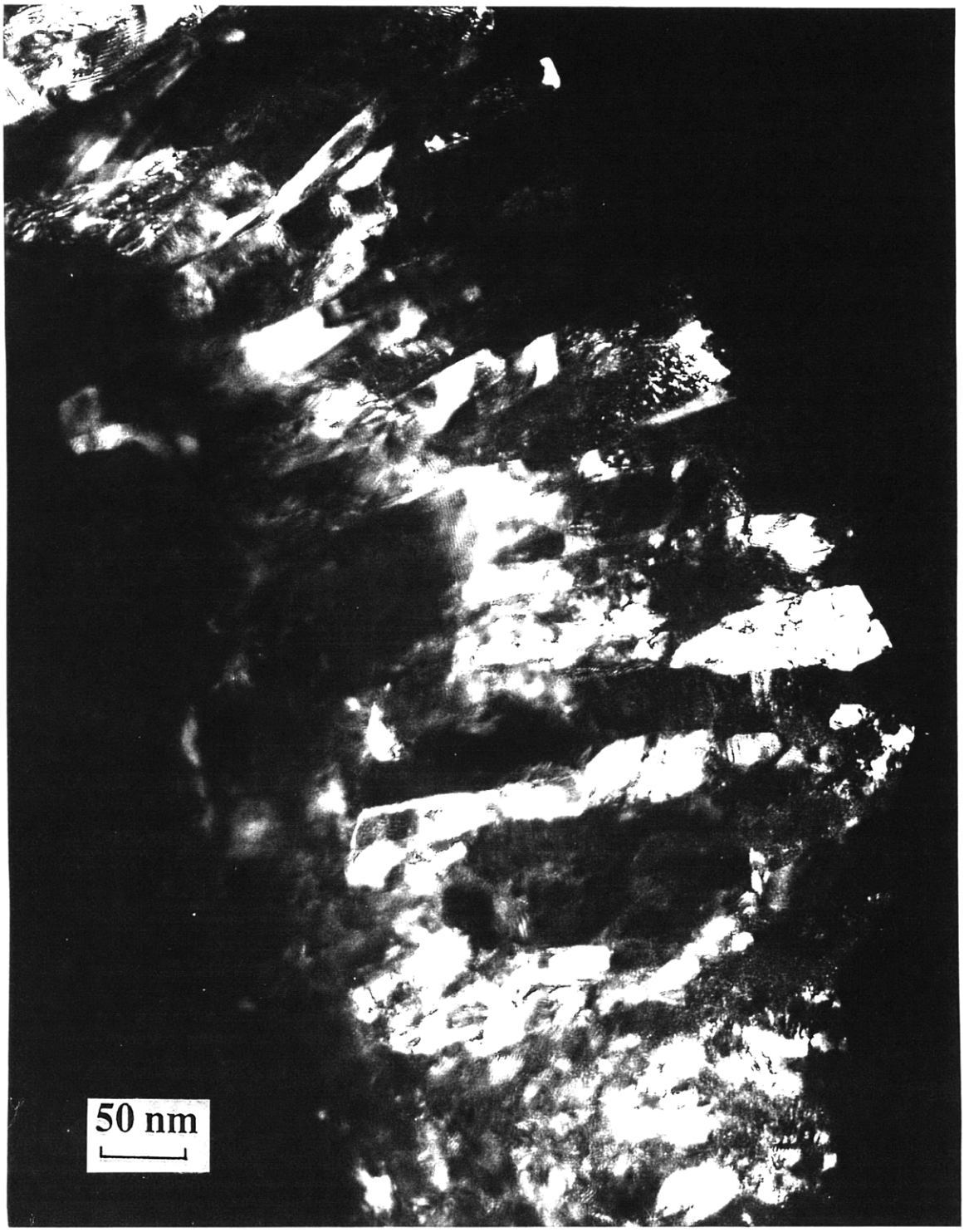

Figure 4.7: TEM cross-section of the first third (approximately 0.5 μm) of zirconia scale on Zr-2.5%Nb, oxidized in the transverse direction 30 min at 1100° F (593° C).

Figure 4.8: Columnar oxide microstructure in oxide grown 3 hours at 1100° F (593° C) in the transverse direction.

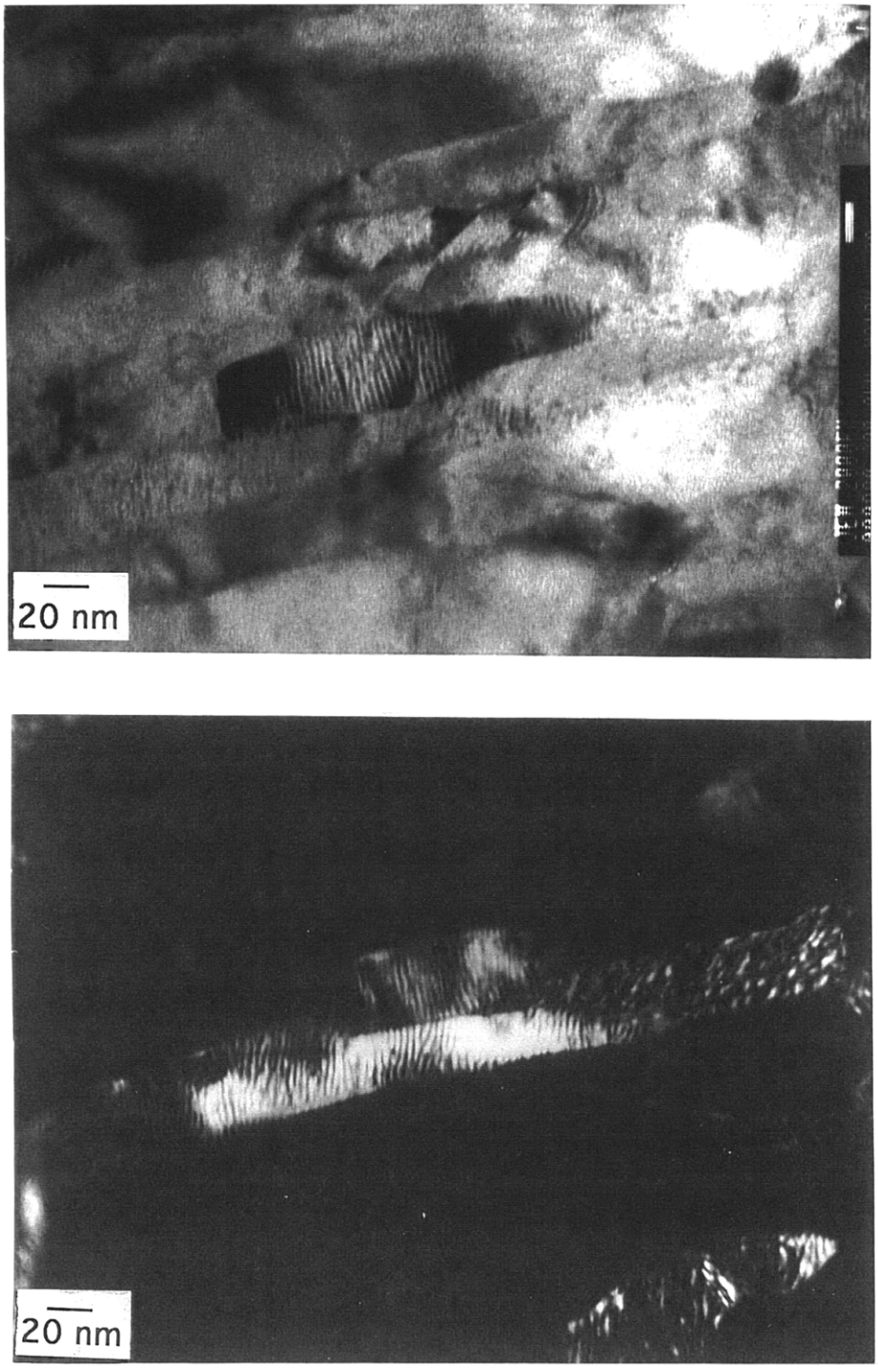

Figure 4.9: Bright-field (top) and dark-field (bottom) TEM images of monoclinic ZrO_2 laths in scale grown on transverse face of Zr-2.5wt%Nb substrate oxidized for 3 hours at 1100° F (593° C).

Variation in width of the laths

The widths of these laths were fairly constant right across the scale (see figures 4.7 and 4.8), but varied slightly with oxidation temperature and substrate orientation. In particular, the grain width averaged 40-50 nm in the scale grown on the longitudinal face for 1 hour at 635° C (1175° F); on the other hand, in the scale grown on the transverse face under the same oxidation conditions, the widths are between 80 and 100 nm [25]; in this case, the influence of substrate orientation stands out, oxidation of the transverse faces resulting in larger average grain widths than on longitudinal faces. The difference is smaller at 1100° F.

Electron diffraction patterns

Figure 4.10 [25] shows a bright-field image of the oxide at mid-scale grown on the longitudinal face for 1 hour at 635° C (1175° F); the accompanying selected area electron diffraction pattern was obtained by using a selected area diffraction aperture encompassing in part the area seen in the micrograph. Indexed rings (marked by arrows) correspond to (-111), (111), (002) for the monoclinic ZrO_2 phase (arrows 1,3,4 respectively), and (111) for either the tetragonal ZrO_2 phase or the orthorombic $6ZrO_2.Nb_2O_5$ phase (arrow 2). The presence of tetragonal or orthorombic phases can be deduced from presence of the (111) ring in the electron diffraction pattern but distinguishing between the two phases is difficult because the major peaks overlap [33]. The electron diffraction pattern shows strong texture in both the monoclinic and tetragonal/orthorombic phases. The fiber axis corresponds to the direction of grain growth. Figure 4.11 proves that the t-ZrO_2 or o-$6ZrO_2.Nb_2O_5$ phase is also detectable for other oxidation conditions, and other substrate directions. It presents a dark-field micrograph from a region approximately 0.5 μm above the interface in the scale grown on a transverse face oxidized 3 hours at 1100° F. It reveals again the diffraction peak of the tetragonal or orthorombic phase inserted between the (111)m and the (-111)m peaks of the monoclinic phase. While the monoclinic phase is overwhelmingly present in both figures 4.10 and 4.11 in the form of the m-Zr elongated grains, it was not found possible

to detect the whereabouts or the morphology of the second phase present in the microstructure. Also, it did not prove possible to deduce any evolution in the texture of the oxide grains from the top of the scale down to the interface using the electron diffraction patterns.

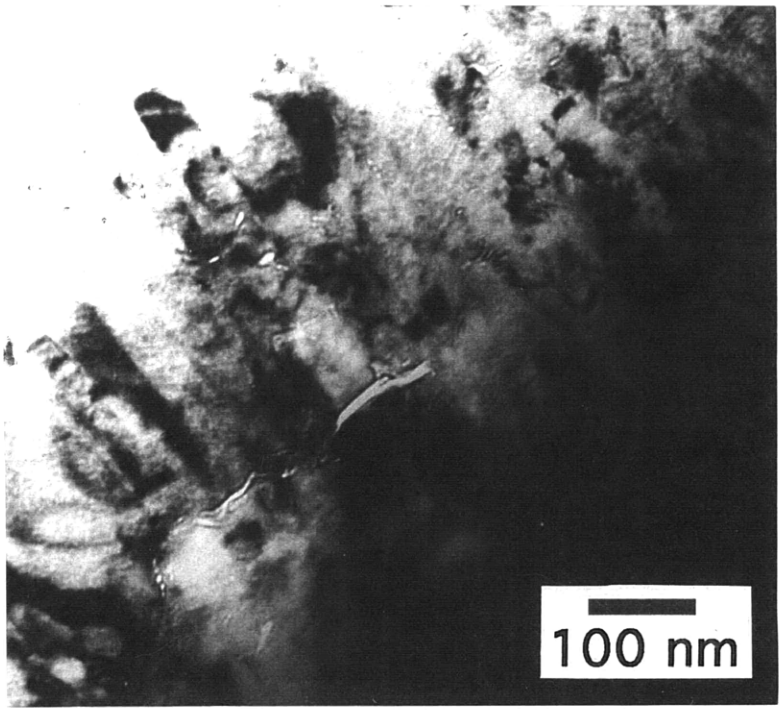

Figure 4.10: a) Bright-field image of the oxide scale close to the interface with the substrate oxidized on the longitudinal face for 1 hour at 1175° F (635° C).

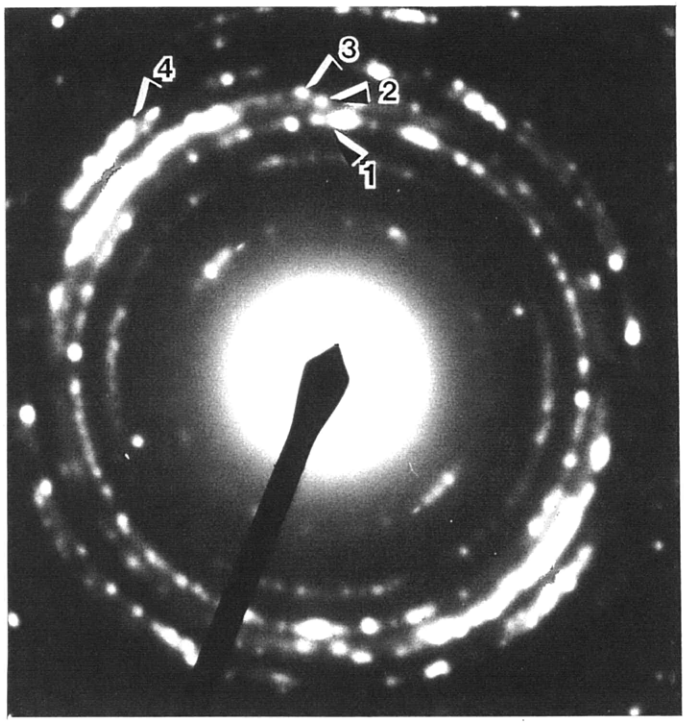

1 (-111)m
2 (111)t
3 (111)m
4 (002)m

Figure 4.10: b) Electron diffraction pattern associated with the image.

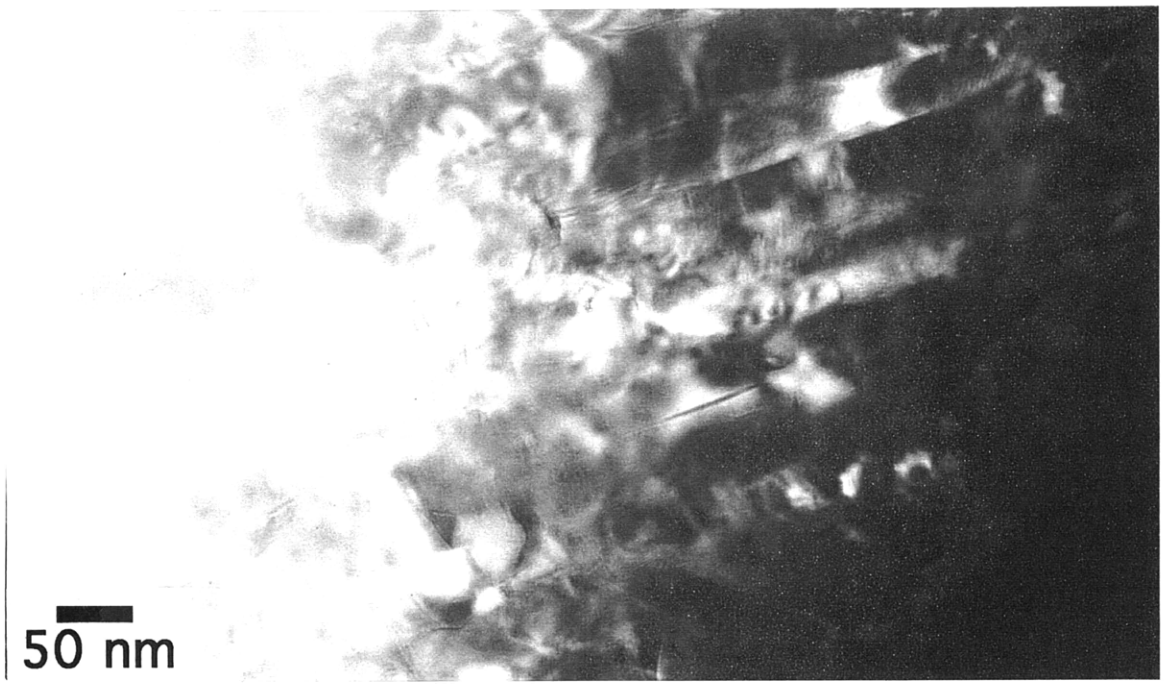

Figure 4.11: a) Dark-field image of the oxide scale about 0.5 μm above the interface with the substrate oxidized on the longitudinal face for 3 hours at 1100° F (593° C).

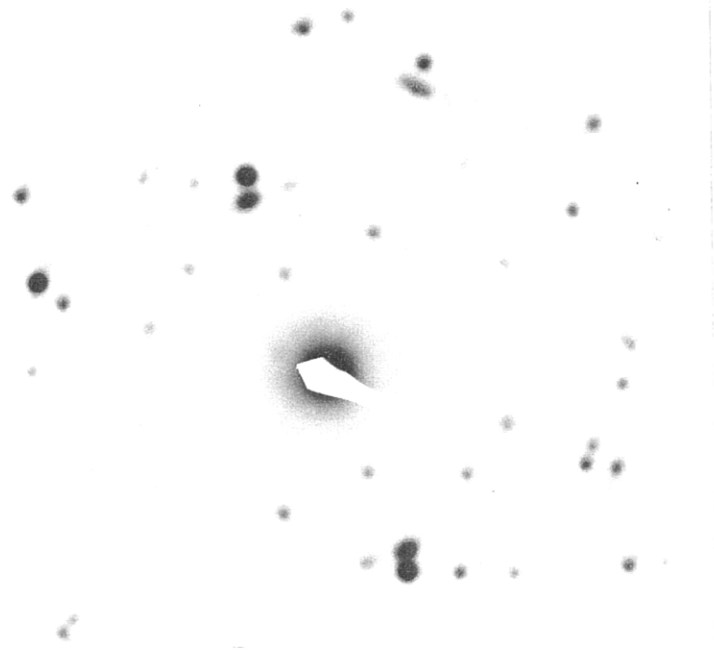

Figure 4.11: b) Electron diffraction pattern associated with the image.

Interface

The columnar structure appears uniform throughout the oxide except near the interface. Figure 4.12 shows an extended view of the interface between the oxide and a transverse alloy face of a specimen oxidized for 3 hours at 593° C (1100° F). To obtain this picture, multiple bright-field images were taken along the interface; the micrographs were digitally scanned, and, using an image analysis software (Adobe Photoshop 4.0), assembled to form a composite map of the interface. The oxide and the metal are seen to be separated by a well-defined interface. This interface is not regular; some parts of the oxide extend deeper into the alloy substrate than others. In fact, the oxide columnar grains and the larger and more equiaxed alloy grains appear to interlock one into the other. There is a transition region 100 to 250 nm beyond the interface, in which the oxide structure is more disordered. In some areas of the interface, the alloy grains appear separated from the columnar oxide grains by apparently amorphous material. Figure 4.13 [25] shows another view of the interface, however for different oxidation conditions: it shows a cross-section across almost all of the oxide scale and its interface with a Zr-2.5wt%Nb substrate oxidized 1 hour at 635° C (1175° F) in room air on a transverse face. The interface between the oxide and the substrate has the same main features as in figure 4.13; it appears scalloped, and exhibits no interfacial cracks or voids. However, it also appears more sharply defined; the amorphous zones noted in figure 4.12 are not visible in figure 4.13. One of the metal grains and several oxide grains are visible, while an interfacial layer between them is not detected (arrows).

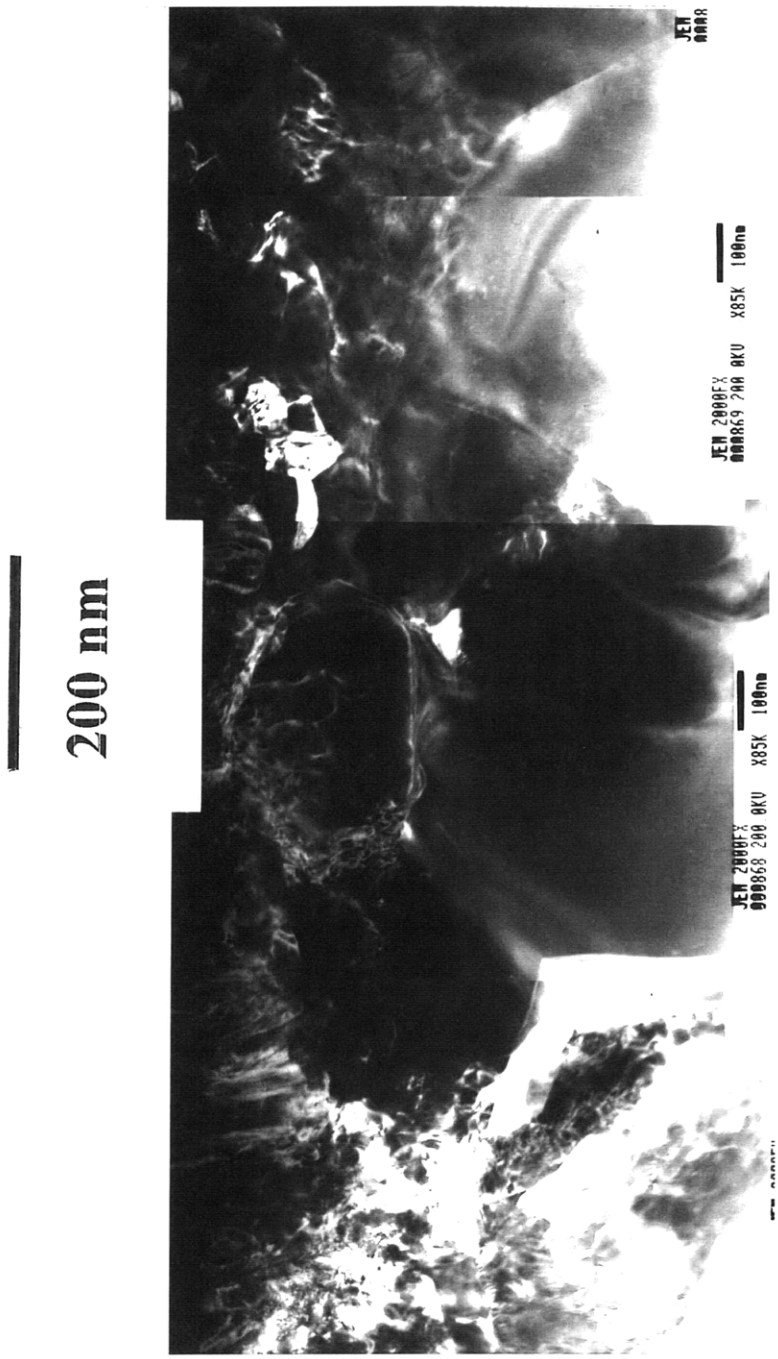

Figure 4.12: Micrographs of the interface between substrate and oxide grown on the transverse face for 3 hours at 1100° F (593° C).

Figure 4.13: a) Bright-field image of interface in a sample oxidized on the transverse face for 1 hour at 1175° F (635° C) [25].

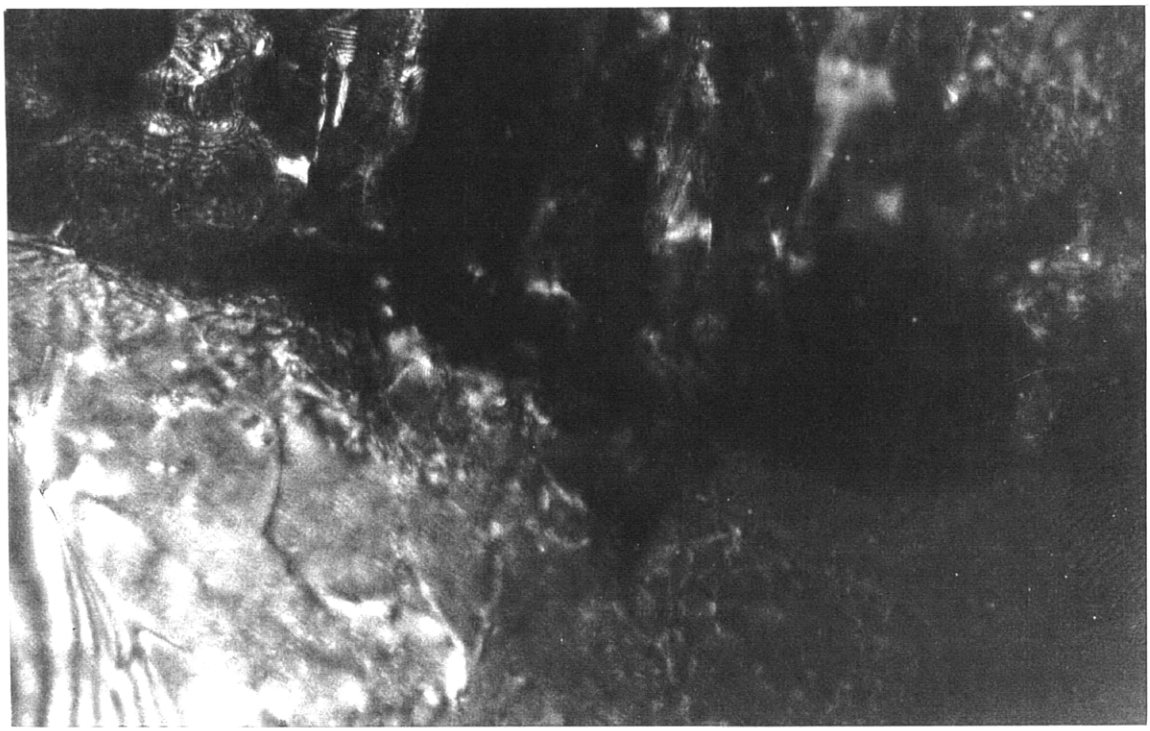

Figure 4.13: b) Corresponding dark-field image [25].

Voids and cracks in the scale

As mentioned before, no cracks or voids were detected in the vicinity of the interface. Figure 4.15 shows, however, that voids and microcracks can be found in the mid-scale. The dark-field image reveals a void in the scale ~1 μm above the interface on a transverse face, oxidized 3 hours at 593° C (1100° F). Dark-field imaging selectively enhances the contrast from voids and is preferred to bright-field imaging because its use largely eliminates confusion between zones of amorphous material and voids. The void (or crack) observed runs perpendicular to the columnar structure. Its length is approximately 100 nm and its width is between 10 and 15 nm. It runs along an elongated feature, a darker triangular zone. A selected area diffraction pattern from this crescent-shaped feature could not be obtained because of the limitation in size of the selective area aperture. It could therefore not be established whether an oxide phase other than m-ZrO_2 was present along the void or microcrack.

Areas of granular oxide.

Although the vast majority of the oxide has a columnar structure, small zones with a more granular appearance were detected amidst the columnar grains. Figure 4.15 shows a bright-field image of the oxide approximately 0.5 μm from the interface with a transverse alloy face oxidized for 1 hour at 635° C (1175° F) [25]. This zone of granular material, which could be amorphous, resembles a remnant of the substrate, as if oxidation were not complete or proceeded differently in this area.

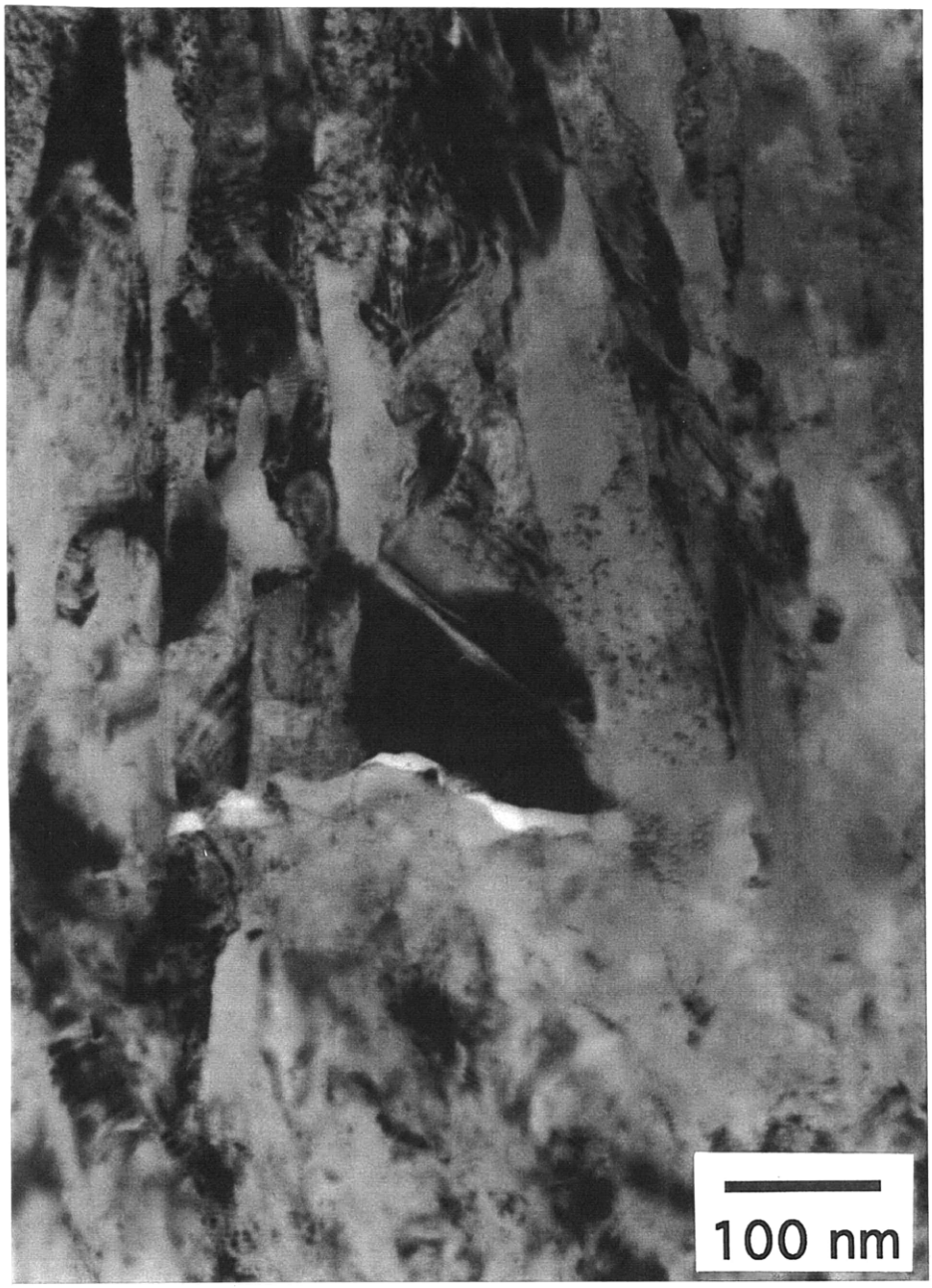

Figure 4.14: Microcrack/void in oxide grown
on the transverse face for 3 hours at 1100° F (593° C).

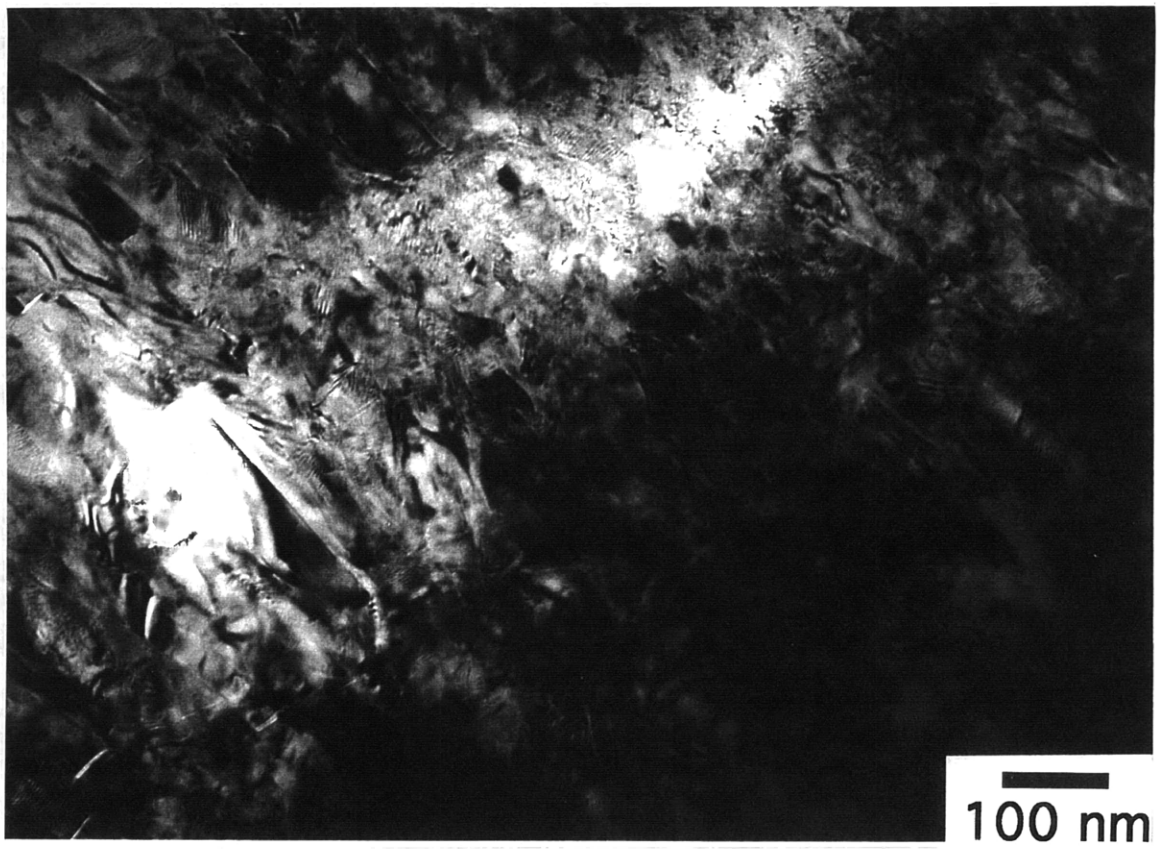

Figure 4.15: Oxide scale close to the interface in sample oxidized 1 hour at 1175° F (635° C) on the transverse face.

4.3.2 STEM Results.

STEM-XEDS analysis detected (figure 4.16) a zone rich in niobium within the oxide. This feature was observed on oxide grown on a transverse face oxidized for 3 hours at 593° C (1100° F). The niobium was detected well inside the oxide, approximately 2 μm away from the interface. In the enlargement, shown in figure 4.17, it appears that this zone consists of clusters containing lath-like grains with a high amount of niobium. The niobium content in the laths was evaluated at 18% (elemental composition). In contrast, other micrographs showed a total absence of detected niobium in adjacent areas of the oxide (figure 4.18). The presence of niobium-enriched zones in the oxide was observed also for other oxidation conditions, such as 1 hour at 635° C (1175° F) , but less consistently.

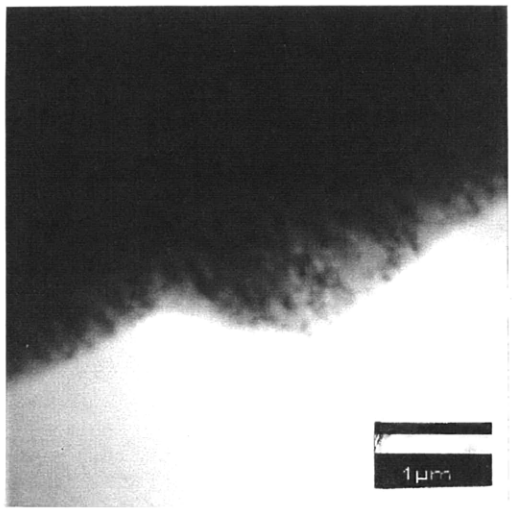

Figure 4.16: a) STEM micrograph of the scale grown on the transverse face for 3 hours at 1100° F (593° C).

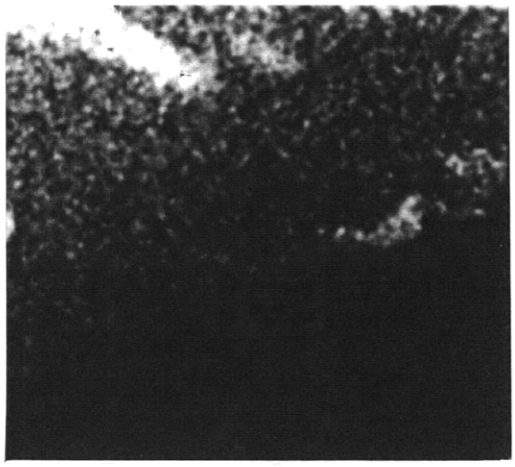

Figure 4.17: b) associated niobium elemental analysis map.

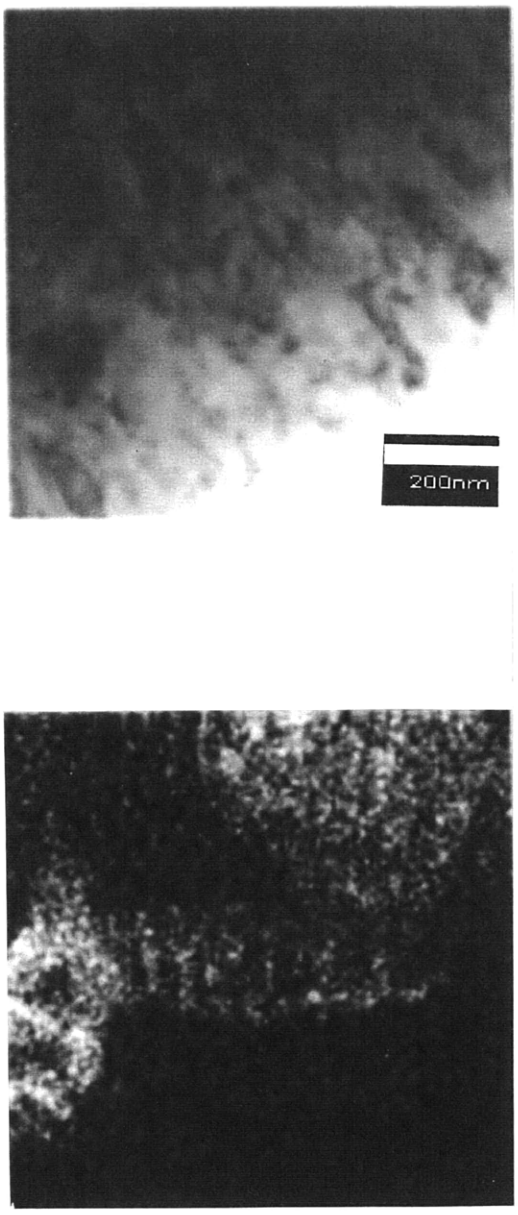

Figure 4.17: Enlargement of figure 11.

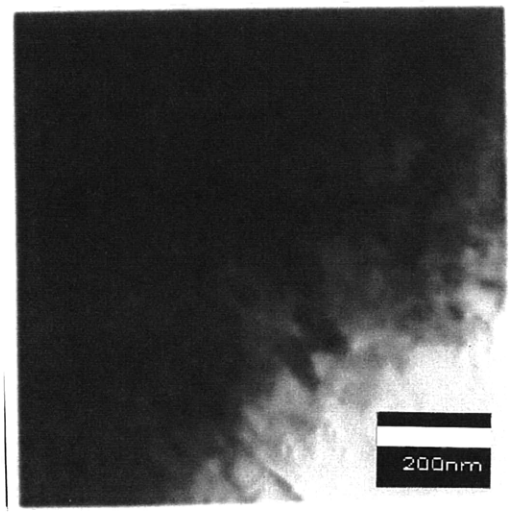

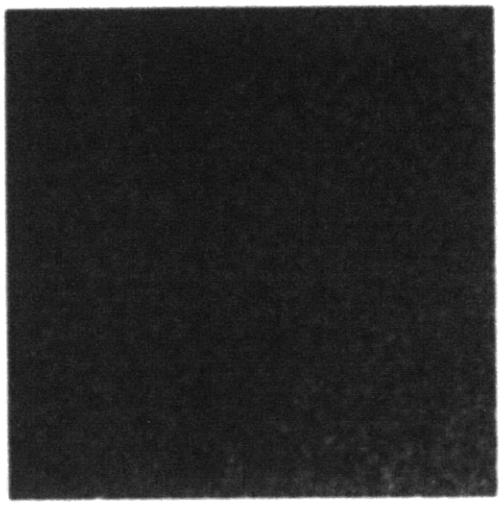

Figure 4.18: a) STEM micrograph of another oxide area in scale grown on the transverse face for 3 hours at 1100° F (593° C).
b) associated niobium elemental analysis map.

4.4 Microstructure of the alloy.

4.4.1 TEM Results.

Morphology

Figure 4.19 shows a bright-field picture of the alloy in a cross-section of the transverse face. The microstructure appears mostly to consist of grains large compared to those in the oxide (dimensions typically of 1 μm versus ~0.1 μm for the oxide). Two types of grains can be distinguished: elongated grains, and grains with a smaller aspect ratio. The elongated grains are parallel to each other, forming a structure that looks like a brick-wall. The elongated direction is perpendicular to the transverse face, so the elongation of these grains is along the forging direction (longitudinal face). Micrographs taken in other areas of the same specimen showed, however, that this arrangement was not as orderly and regular everywhere in the substrate; the elongated grains appear distributed in a more random fashion among more equiaxed grains. A common feature, however, is the clear distinction between two categories of grain shapes: equiaxed, and elongated.

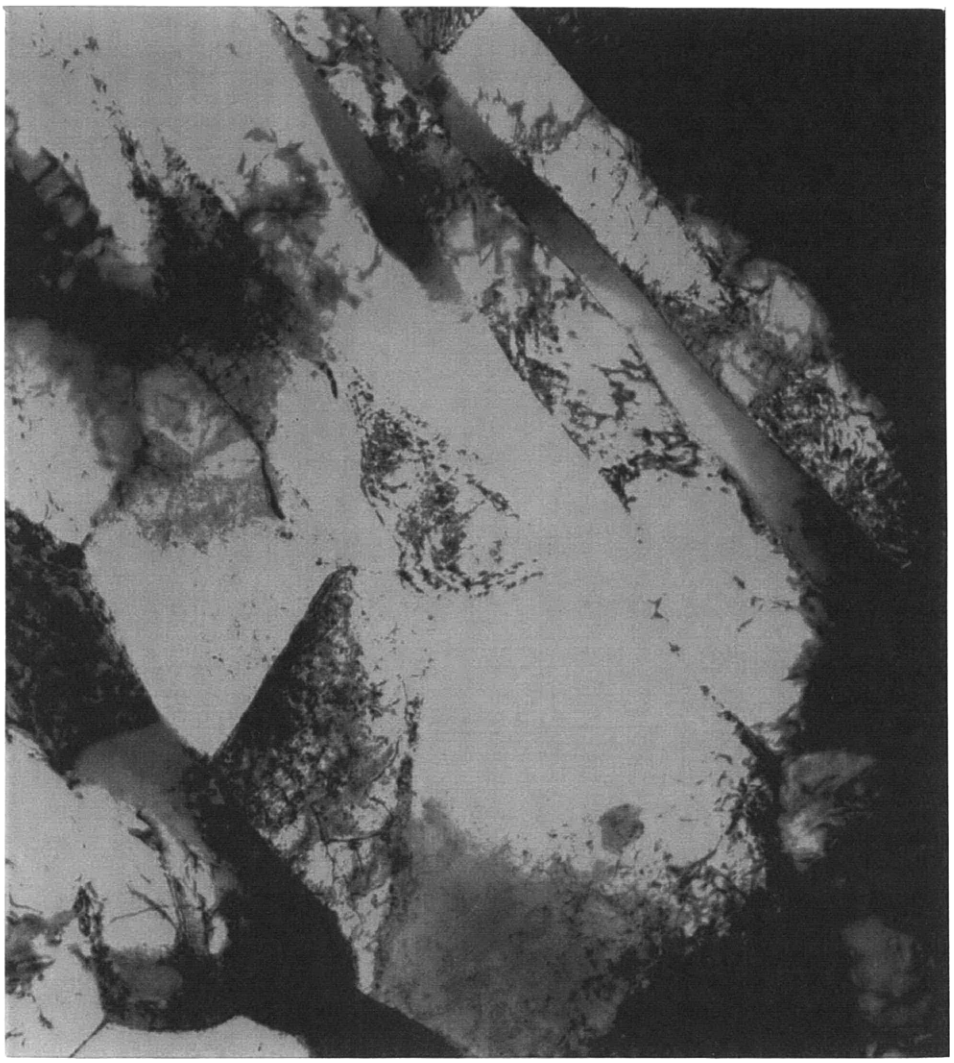

Figure 4.19: Bright-field micrograph of the alloy on the transverse face of a Zr-2.5wt%Nb oxidized specimen.

Dimensions of the alloy grains

The elongated grains have generally a width between 0.2 and 0.4 μm, and a length between 1 and 2 μm. The more equiaxed grains still have generally a rectangular aspect, with the long dimension aligned with the length of the elongated grains; their length is 1 to 2 μm, while their width is typically 1 to 1.5 μm (figures 1 and 2). The dimensions of both types of alloy grains are, again, much larger than those of the oxide. Both features appear identically in cross-sections of both longitudinally and transversely sectioned samples, from which it is concluded that the elongated grains are sections of complete sheaths surrounding the equiaxed grains.

Electron Diffraction Patterns

Diffraction patterns reveal more about the nature of the alloy grains. Figure 4.20 shows a equiaxed grain and its corresponding diffraction pattern, and figure 4.21 an elongated grain and its corresponding diffraction pattern. Both images are in dark-field mode. Although the two grains are adjacent, their internal contrast is very different. While the grain in figure 4.20a is internally featureless, contrast from the grain in figure 4.21a is moffled. It is not clear whether the dramatic contrast difference of aspects arises from the image conditions or the surface topography. In the latter case, the grain materials could be structurally or chemically different, or have different crystalline orientations, and so be affected differently by the erosion of ion-milling during specimen preparation. In both cases, the selective area aperture, which delimits the area contributing to electron diffraction, was carefully chosen to fall well inside each grain, to ensure that the diffraction pattern comes from the grain itself, and not any other element present in the microstructure. The diffraction pattern of the equiaxed grains indexes to α-Zr phase (hexagonal-close-packed), while the diffraction pattern of the elongated grains indexes to a β-Zr phase (body-centered cubic). The two phases can therefore be readily distinguished according to their grain shapes in section, and it is concluded the β-Zr sheaths have formed around bundles of α-Zr grains.

Figure 4.20: a) Bright-field micrograph of a rounder Zr-2.5wt%Nb alloy grain.

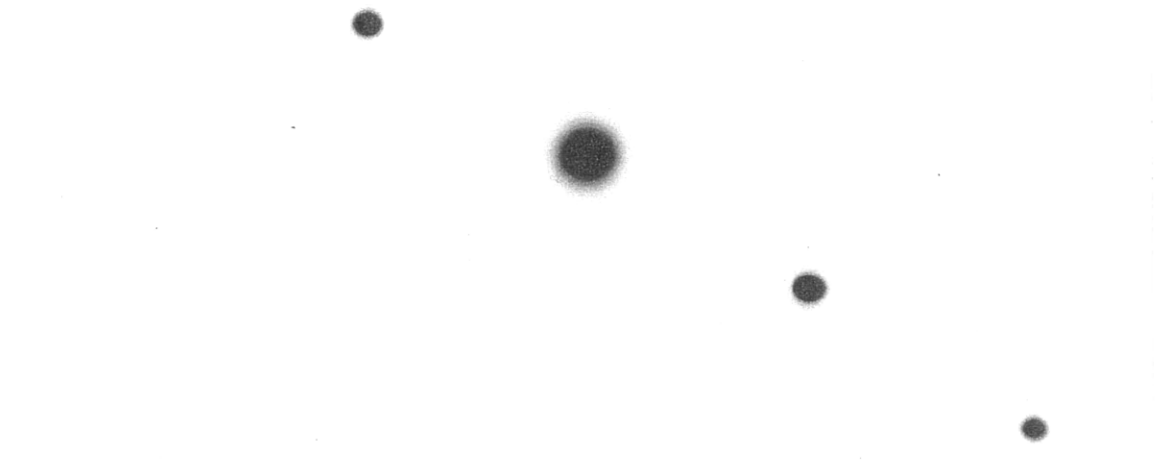

Figure 4.20: b) associated diffraction pattern

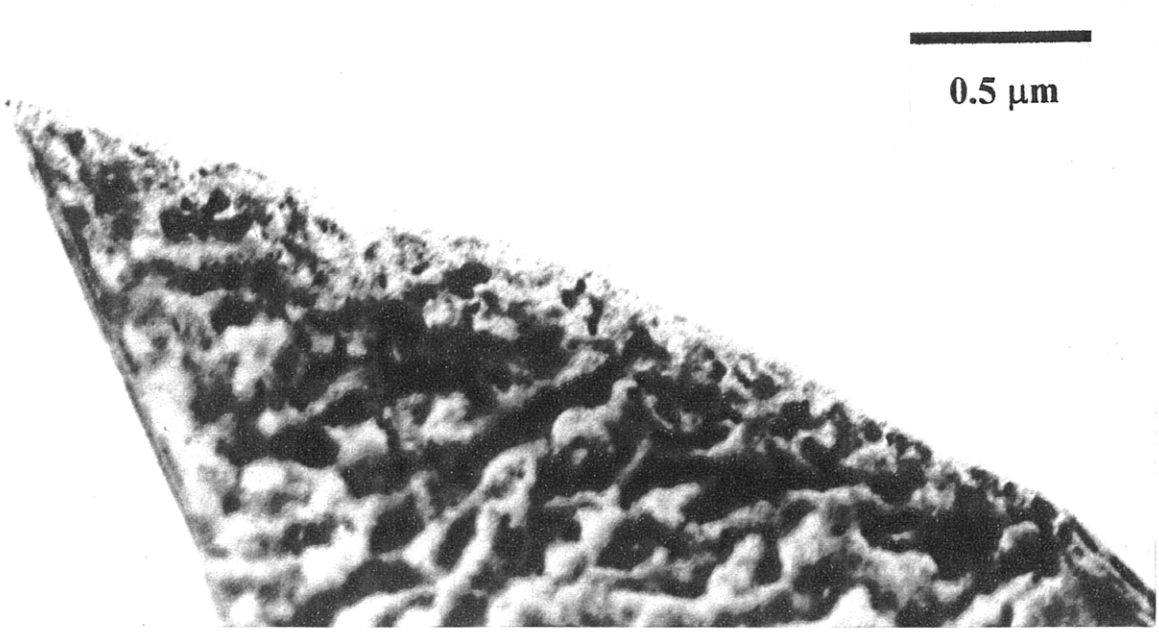

Figure 4.21: a) Bright-field micrograph of an elongated Zr-2.5wt%Nb alloy grain.

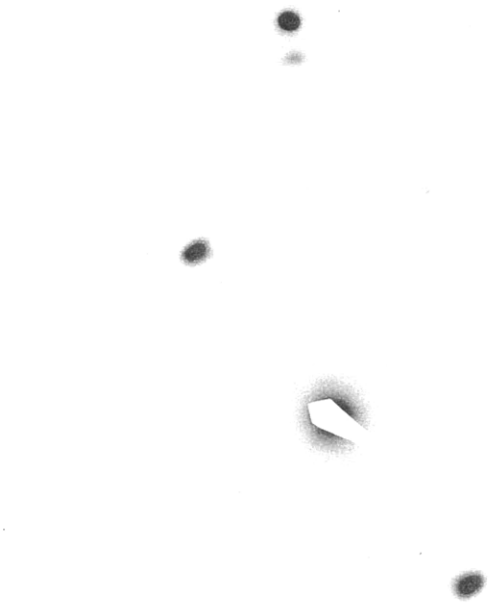

Figure 4.21: b) associated diffraction pattern.

Lath structures in alloy grains

Observations made in the alloy, in both the transverse and longitudinal sections and for specimens oxidized under various conditions, show that the alloy located deep in the substrate remains unaffected by the oxidization process. However, figure 4.22 shows a strong-beam dark-field image of the alloy near the scale grown on a transverse face for 3 hours at 593° C (1100° F). A large alloy grain is flanked by two groups of grains with parallel lath-like features. The two groups exhibit completely different lath directions. These laths have a morphology distinct from that of the oxide columnar grains, yet they are not characteristic of the alloy either, which has larger grains. It is possible that the region imaged falls in a zone of suboxide formation, or represents the eutectic decomposition microstructure.

Figure 4.22: Dark-field micrograph showing lath-like sheaths in the Zr-2.5wt%Nb alloy.

4.4.2 STEM Results.

The use of STEM provides the advantage of simultaneous imaging and elemental analysis of the alloy microstructure, in particular revealing Nb enrichment. Figure 4.23 shows the arrangement of lath-like grains in columns interspaced by layers of more equiaxed grains. The accompanying elemental analysis revealed that the elongated grains are enriched in niobium. Figure 4.24 shows the same analysis conducted in another area of the alloy in the specimen. The grain arrangement appears less orderly than in figure 4.23, and the columnar sequence of elongated grains is disrupted. The elemental map shows nonetheless that the grains with an elongated shape contain more niobium than the equiaxed ones. The distinction between two types of alloy grains found by TEM contrast and diffraction is therefore confirmed compositionally by STEM. The STEM results provide the further piece of information that the elongated grains, identified as β-Zr grains by TEM diffraction, are also enriched in niobium. The niobium content is estimated at close to 18 % in these β-Zr grains. The niobium content in more equiaxed α-Zr grains was also investigated, and also Nb segregation to grain boundaries between adjacent α-Zr grains. No appreciable Nb content was detected in either location. In summary, the main information provided by STEM was to reveal the high niobium content of the β-Zr grains, and to confirm the regular brickwall grain arrangement in the Zr-2.5%Nb alloy.

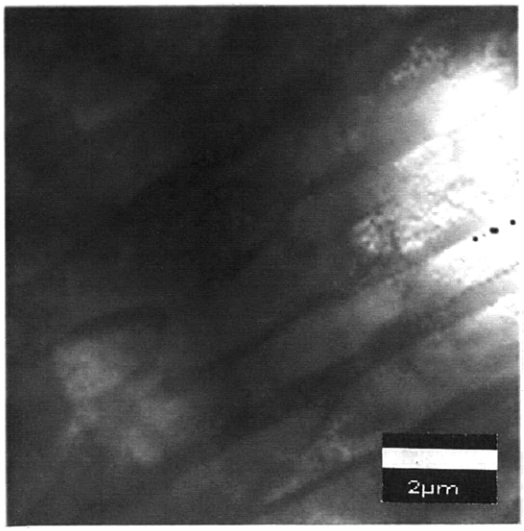

Figure 4.23: a)STEM micrograph of the Zr-2.5wt%Nb alloy on the transverse face and,

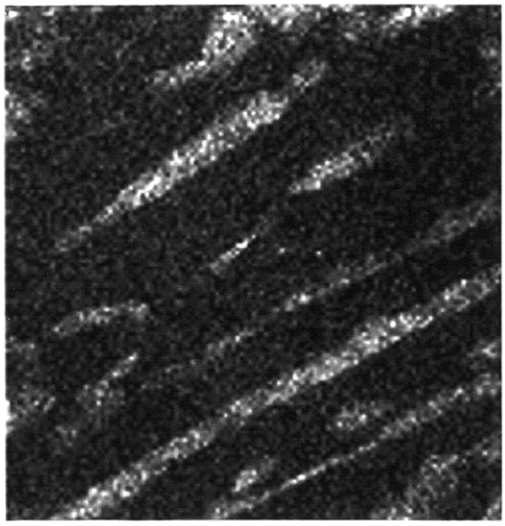

Figure 4.23: b) associated niobium elemental analysis map. Orderly lath arrangement.

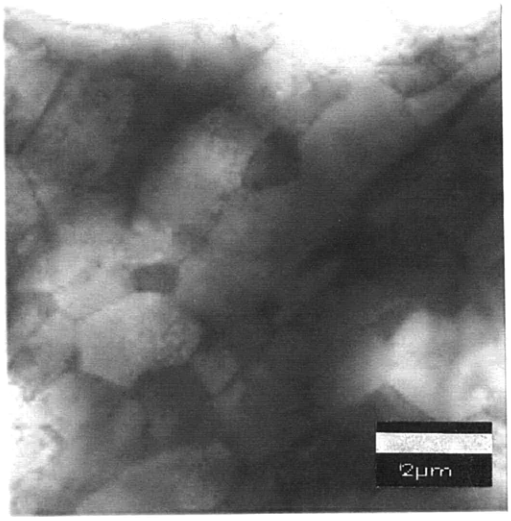

Figure 4.24: a)STEM micrograph of the Zr-2.5wt%Nb alloy
on the transverse face and,

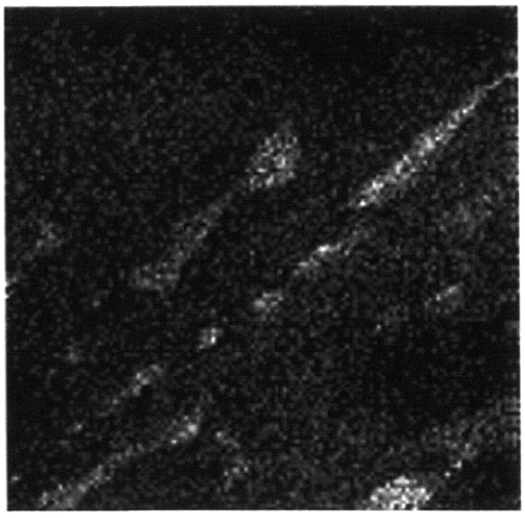

Figure 4.24: b) associated niobium elemental analysis map.
Disordered lath arrangement.

Chapter 5:

Discussion

5.1 Microstructure of the alloy.

TEM observations in the alloy showed that the substrate is composed of monolayers of elongated grains separated by multilayers of more equiaxed grains arranged in a brickwall structure, as shown in figure 5.1. Results obtained by TEM diffraction showed that the more equiaxed grains were α-Zr (hexagonal-close-packed) and the elongated grains β-Zr (body-centered-cubic). STEM analysis confirmed that the α-Zr contained 1% niobium, whereas β-Zr grains accomodated up to 20% Nb. The presence of β-Nb, which derives from the metastable β-Zr (see phase diagram for niobium-zirconium in figure 5.2), was not detected in the alloy. Its undetected presence is very improbable, since its ~85%Nb content makes it easily recognizable by STEM analysis. The microstructure of the Zr-2.5%wtNb differs therefore from that described by Lin [24]; however, this is not surprising, since the alloy preparation condition (different in our study from those for the alloy in nuclear applications) play a predominant role in evolution of the resulting microstructure. It is also clear from figure 5.1 that the substrate is anisotropic: on the longitudinal face, the sheaths of β-Zr run parallel to the surface, whereas they emerge normal to the transverse face. The similar morphologies observed in both longitudinal and transverse sections suggest that the α-Zr grains are surrounded by complete β-Zr sheaths. The anisotropy of the substrate microstructure can therefore account for different oxidation mechanisms on the transverse and longitudinal faces.

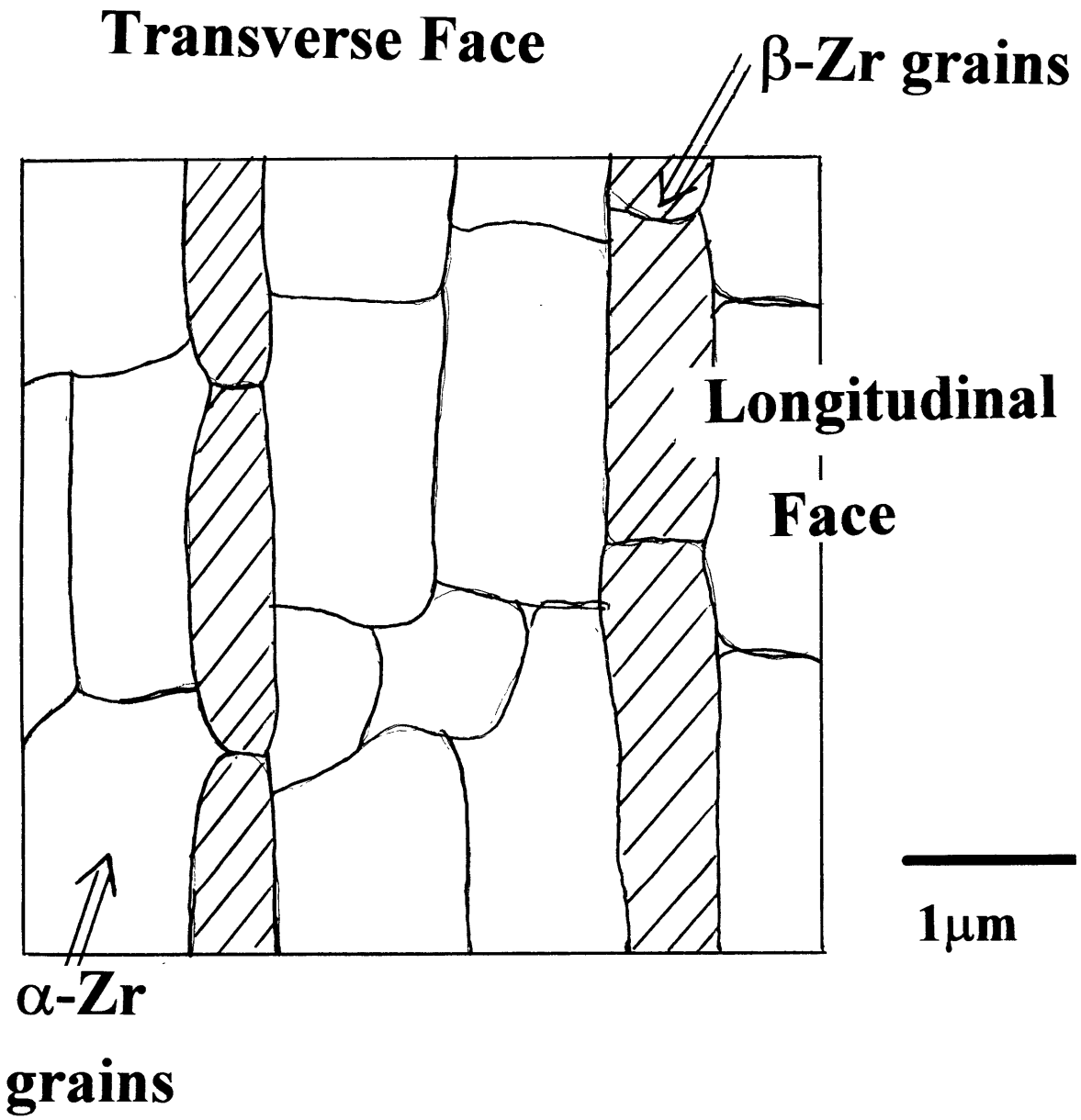

Figure 5.1: Schematic representation of the alloy microstructure.

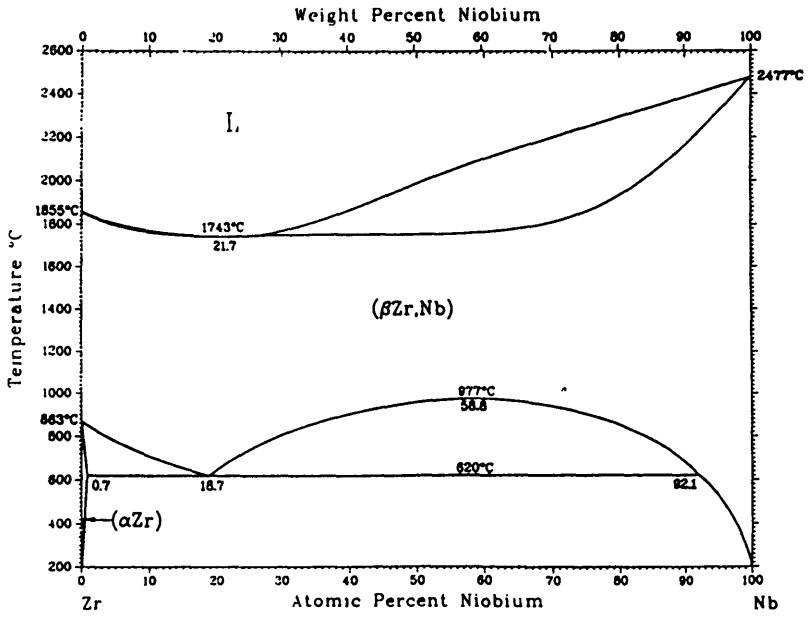

Figure 5.2: Zr-Nb phase diagram [32].

5.2 Microstructure of the oxide grown on alloy substrate.

TEM observations revealed the columnar structure of the oxide. The TEM diffraction patterns showed that the oxide grains were mostly monoclinic m-ZrO_2 and had a strong orientational texture. The columnar oxide grains grown on transverse alloy faces were consistently observed to be wider than the oxide grains grown on longitudinal alloy faces. Near the interface, the oxide microstructure appears more complex. Zones of amorphous material were sometimes observed, and identified by dark field microscopy. A crystalline interfacial layer with grain boundaries was also observed, the grains of which were 250-300 nm across and typically extended along the width of several oxide grains; these grains extended approximately 100 nm into the metal, from which they were distinguished by the larger diameter of the adjacent or underlying alloy grains. Both interfacial layers suggest there could be a suboxide, but it is also possible that they represent regions where the β-Zr sheath has fortuitously arrived at the oxide/alloy interface and oxidized as that interface moves down into the alloy. STEM pictures of the oxide revealed areas rich in niobium retained further up in the oxide layer; these may be remnants of oxidized β-Zr sheath. Diffusional transport of Nb may explain why the niobium-enriched zones appear rare and isolated in the scale, while they are omnipresent in the alloy as β-Zr sheaths. These remnants, observed in samples oxidized at 593° C (1100° F), have at least a partially amorphous appearance. At the higher temperature, 635° C (1175° F), the crystalline interfacial layer was more frequently observed. In the alloy immediately below the interface, several groups of parallel laths were observed at the transverse alloy face. Their width and elongated shape differ from those of the alloy grains, and also of the columnar oxide grains. This type of morphology, found directly below the interface with the oxide scale, has also been observed previously in Zircalloy-4 by Newcomb [22]. ESEM cross-sections images revealed what appears to be an oxygen diffusion zone extending below the oxide scale far deeper into the alloy substrate. The possibility of modifications of the Zr-2.5Nb alloy below the interface cannot therefore be excluded.

5.3 Transport mechanisms.

Oxidation of the zirconium alloy substrate takes place at the metal/oxide interface, so the earliest formed oxide is near the the oxide/gas interface. According to Wagner theory [31], if sufficient oxygen gas is available at the oxide surface, the rate of oxidation at high temperatures will be limited by solid-state diffusional transport of the reactants or electrons through the scale. As the scale grows in thickness, the length of the diffusion paths increases, and the reaction rate decreases with time. Correspondingly, a gradient in the partial pressure of oxygen exists between the atmosphere (at the surface of the scale) and at the interface with the alloy. At the scale/alloy interface, the partial pressure is the decomposition pressure of the oxide. Together with the chemical potential, a gradient of the electrical potential also must be taken into account: the flux of metal cations, oxygen anions, and electrons, all with different mobilities, creates a charge distribution across the scale. The transport of the reactants may take place by various mechanisms, e.g. diffusion through the lattice and along grain boundaries. Also the scale growth will affect these diffusion processes. In pure zirconium oxide, the transport of oxygen occurs very probably via movement of oxygen vacancies in the lattice or along oxide grain boundaries. An equilibrium exists between the oxygen gas pressure, the oxygen vacancy content, and the concentration of electrons. Because Zr^{4+} is known to be a slow-diffusing species, most of the transport is very probably caused by oxygen vacancies and free electrons.

The incorporation reactions for niobium into the oxide, especially upon oxidation of the β-Zr grains (~20%Nb), can be written as:

$$Nb_2O_5 \text{ (in } ZrO_2) \rightarrow 2\ Nb_{Zr}^{\bullet} + O_i'' + 4O_o^{x} \qquad (5.1)$$

$$Nb_2O_5 + V_o^{2\bullet} \text{ (in } ZrO_2) \rightarrow 2\ Nb_{Zr}^{\bullet} + 5\ O_o^{x} \qquad (5.2)$$

For dissolution of Nb_2O_5, in which the niobium ions have a valence of +5, a substitional niobium ion has one positive effective charge, $Nb_{Zr}^{\bullet}$. But near the alloy/scale interface, where the partial pressure of oxygen, set by the Zr/ZrO_2 equilibrium, is very small, lower valence states of Nb may result; hence, also,

$$NbO\ (in\ ZrO_2) \rightarrow Nb_{Zr}'' + V_o^{2\bullet} + O_o^x \qquad (5.3)$$

$$NbO_2\ (in\ ZrO_2) \rightarrow Nb_{Zr}^{\bullet} + 2\ O_o^x \qquad (5.4)$$

According to the incorporation reactions (equations 5.1-5.4), the niobium will either decrease (equations 5.1, 5.2), increase (equation 5.3), or bring no change (equation 5.4) to the oxygen vacancy content in the oxide. Also, as the scale grows, the oxygen pressure increase which subsequently occurs in older regions of the oxide can change the incorporation reactions. If we consider the dissolution of Nb_2O_5 in ZrO_2 to be predominant, the addition of niobium will then decrease the number of oxygen vacancies, and slow down the diffusion of oxygen into the scale. Accordingly, the oxidation of α-Zr grains will proceed faster than will oxidation of β-Zr grains. This concept provides a good interpretation of the TEM and STEM observations showing inclusions rich in niobium inside the scale. These inclusions resulting from β-Zr grains, are surrounded by faster growing oxide from the α-Zr grains. On the transverse face, the β-Zr sheaths are arranged perpendicular to the transverse face, so that ZrO_2 low in Nb will always extend from the scale/alloy interface to the scale/gas interface in most regions, which implies an availability of more rapid paths for diffusion of oxygen through the scale grains, and also that the oxide products of the β-Zr grains will always be incorporated in the scale. In contrast, the β-Zr sheaths are parallel to the surface on the longitudinal face: the scale growth may encounter a sheath or not, and if not will consume only the α-Zr grains with small Nb content. But, if at least one β-Zr sheath is encountered, the oxygen must therefore diffuse through zones alternately rich and poor in oxygen vacancies over more extensive lateral regions (see figure 5.2). This difference may explain the difference in oxidation kinetics and in columnar oxide grain widths observed on the two faces. However, it is rather remarkable that the results showed that the oxides grown on the transverse and longitudinal faces have altogether similar microstructures. This may due to the observed less than orderly arrangement of the alloy grains, which lessen the barrier effect of the oxidized β-Zr sheaths. Also, other transport mechanisms than lattice transport of oxygen vacancies may be significant, such as diffusion along the oxide grain boundaries, where the effect of dissolved niobium may be different.

5.4 Oxidation reactions.

The overall driving energy for the oxidation reaction is the free energy change associated with the formation of an oxide. For zirconium, it is the free energy change from Zr to ZrO_2. Niobium forms a stable monoxide NbO and dioxide NbO_2, in addition to the highest oxide, Nb_2O_5, which exists in several polymorphic forms. As a result, a larger number of different reaction products may be formed in the oxidation of the niobium, and this possibility renders the oxidation mechanism even more complex. Free energy diagrams [34] show that zirconium oxide is considerably more stable than the niobium oxides. Also, the monoxide NbO and dioxide NbO_2 are thermodynamically more stable than Nb_2O_5. A direct consequence of the free energy changes is that the niobium oxides will form more easily from the β-Zr grains (containing 20% niobium) than from the α-Zr grains (~1% niobium). Also, as the oxide scale grows, competition for oxygen depletion at the alloy/scale interface may prevent the formation of Nb_2O_5 first, then that of all the niobium oxides. Wagner oxidation diffusion theory [1] analyzes this case; when the activity of oxygen becomes too low to form any niobium oxide, the niobium cations will then diffuse into the alloy from the scale/metal interface. As oxidation proceeds, the concentration of Nb in the alloy will increase, and formation of niobium oxide might then occur. This oxidation sequence does not, however appear to occur in practice. The microanalysis results in the alloy and the oxide did not indicate a perceptible enrichment of niobium content near the interface. In the oxide, the microstructure is uniformly columnar and monoclinic m-ZrO_2, which can accomodate ~5% Nb_2O_5 at 1400° C (figure 5.3), which extrapolates to ~1-2% Nb_2O_5 at 635° C. This represents a ~2-4% Nb cation fraction dissolved in the oxide, which is roughly the overall composition of the alloy. In addition, the ZrO_2-Nb_2O_5 phase diagram (figure 5.3) shows that the orthorombic compound $6ZrO_2.Nb_2O_5$ can form and accomodate 15% Nb_2O_5 (~30% Nb cation fraction), without any formation of Nb_2O_5. This may explain why no pure niobium oxide phase grains were detected in the scale, whereas the microstructural results showed the

presence of niobium-enriched areas inside the scale. The latter may comprise $6ZrO_2$. Nb_2O_5 and ZrO_2, which could result from the oxidation of the alloy β-Zr grains containing up to 20% Nb, and account for the extra diffraction rings formerly attributed to t- ZrO_2 . Furthermore, excess niobium in the oxide from oxidation of the β-Zr sheaths can diffuse in the neighboring ZrO_2 to reduce proportion of $6ZrO_2$. Nb_2O_5 in the ($6ZrO_2$. Nb_2O_5 + ZrO_2) two-phase region.

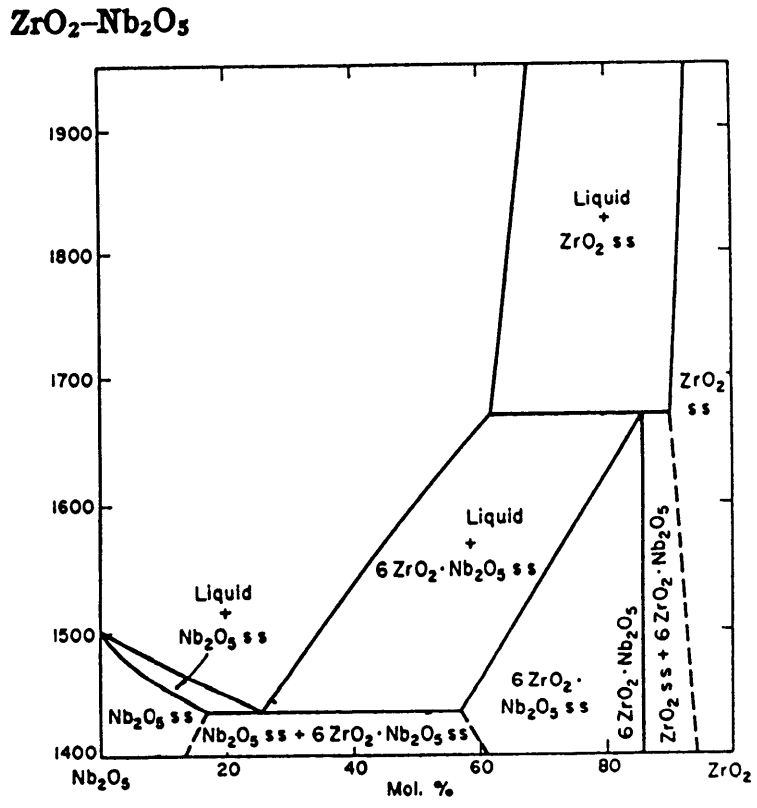

Figure 5.3: ZrO_2-Nb_2O_5 phase diagram [33].

5.5 Potential orthopaedic applications.

The relative absence of gross defects and the highly columnar oxide microstructure are encouraging results for its orthopaedic applications use. The columnar structure of the oxide appears efficient in preventing the propagation of cracks in the oxide parallel to the oxide surface. Indeed, the microcracks that are observed extend no more than three oxide-lath widths. Figure 5.4 shows how the columnar structure may stop the cracks. It is interesting to note that cracks along the columnar direction were not observed in the scale, which suggests a strong cohesion of the parallel grains. The cohesion may also be assisted by the compressive stresses in the oxide measured by in situ X-ray diffraction by Treska [25]

ESEM results revealed that the oxide scale formed at 600° C for 6 hours in room air has a fairly flat top surface, while its interface with the Zr-2.5%wtNb alloy substrate is wavy, consistent with an inward oxide growth mode for zirconia scales; the inward progression of the scale therefore leaves the initial protective oxide layer unchanged once formed, and the subsequent oxidation processes at the scale/substrate interface are those responsible for the new oxide scale. This is an advantage over materials such as nickel alloys, on which the scale grows in the outward direction; in this case, cracking and roughening at the surface can result from preferential grain-boundary diffusion paths and internal formation of oxide at oxide grain boundaries. On the other hand, the scale continually inherits microstructural features from the alloy as it consumes the alloy, for example the variation in Nb content represented by the two alloy phases and grain boundaries in the alloy. Indeed, the truncation of the m-ZrO_2 columnar grains at the observed length may be attributable to the influence of inherited alloy microstructure.

The observation of the defect microstructure at the very top surface of the oxide was not feasible, because of difficulties in the specimen preparation; obtaining a very thin area in the oxide demands extensive ion-milling, and since the nickel material plating the specimen surface is milled away faster than the oxide, its complete removal at the edge of the thin area removes the certainty of observing the very top surface of the scale. For the chosen oxidation conditions of the Zr-2.5Nb alloy substrate, in both the

transverse and longitudinal directions, ESEM and TEM microstructural observations showed a largely intact 2-4 μm thick oxide scale devoid of porosity. The presence of porosity could indicate an onset of breakaway oxidation during the scale formation. The observed oxide is therefore clearly the compact black oxide type, which is preferred for orthopaedic applications to the porous white oxide.

The adhesion of the oxide layer to the Zr-2.5%Nb alloy under cyclic loading is crucial for its use in orthopaedic devices. All observations at the interface of the oxide with the alloy suggest a highly adherent scale. For example, TEM results for oxide grown on both alloy faces and various oxidation conditions show mostly a direct well-behaved uninterrupted interface between the oxide and the alloy, with no intervening layer. Also, the observed faceting of the interface at the columnar oxide grains may confer an additional advantage, since the oxide grains and the metal grains mechanically interlock into each other. The interface also exhibits no interfacial cracks or voids. These are definitely encouraging results with implications for the mechanical resistance of the scale to fracture and spallation.

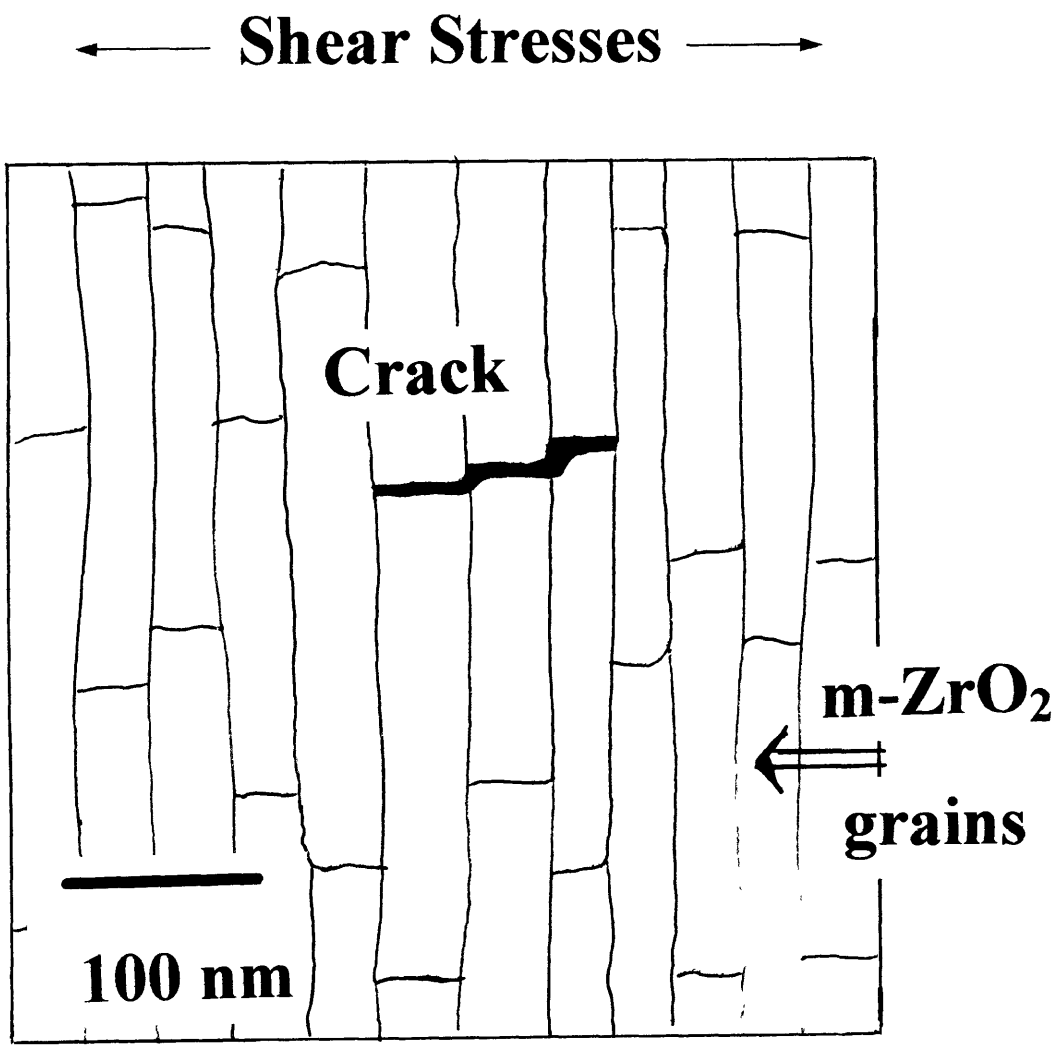

Figure 5.4: Crack propagation in the scale.

Chapter 6

Conclusions

- The oxide grown on a Zr-2.5wt%Nb substrate has a highly columnar structure. It is almost entirely composed of narrow monoclinic zirconia grains with preferential growth orientation along the c-axis.

- The alloy substrate presents different microstructures on the longitudinal and transverse faces, due to sheath arrangements of the β-Zr grains. However the oxide exhibits essentially identical microstructures when grown on the two faces, and the alloyed niobium is accomodated without widespread formation of second phases.

- The interface between the scale and the alloy is direct and well-behaved, and the scale is highly adherent. No cracks or voids were detected at the interface.

- The columnar scale morphologies appear to confer a high resistance to propagation of lateral cracks.

- The scale grown on the zirconium substrate therefore forms a barrier of high integrity against wear in load bearing surfaces for orthopaedic implants.

- Future work could help identify the phases present in the oxide in addition to the predominant monoclinic zirconia, particularly in zones richer in niobium. It would be useful also to investigate what governs the columnar grain lengths, for example the potential role of inherited alloy microstructure.

References

[1] J. Davidson, C. Asgian, A. Mishra, and P. Kovacs. Zirconia (ZrO2)-Coated Zirconium-2.5Nb Alloy for Prosthetic Knee Bearing Applications, Bioceramics, Volume 5, p.389.

[2] J. Davidson, A. Mishra, R. Poggie and J. Wert. Orthopaedic Transactions, 1992.

[3] M. Spector. Prostheses: Materials, Design, and Strategies for Implant Fixation, Orthopaedic Knowledge Update 3, Amer. Acad. Orthop. Surg., 1990, p.186.

[4] M. Spector. Prostheses: Materials, Fixation and Design, Orthopaedic Knowledge Update 4, Amer. Acad. Orthop. Surg., 1993, p.245-246,253.

[5] A. Bartolozzi, J. Black. Serum and urine chromium levels in patients following total hip arthroplasty, Biomaterials, 1985, 6:2.

[6] C. Mintzer, D. Robertson, S. Rackemann, F. Ewald, R. Scott, and M. Spector. Bone Loss in the Distal Anterior Femur After Total Knee Arthroplasty, Clinical Orthopaedics, Nov. 1990, Volume 260, p. 135.

[7] D. Robertson, C. Mintzer, B. Weissman, F. Ewald, M. Leboff, and M. Spector. Distal Loss of Femoral Bone following Total Knee Arthroplasty, The Journal of Bone and Joint Surgery, 1994, p.66.

[8] E. Wachtel, P. Villars, A. Armini, and M. Spector. Tribology of Alumina and Diamond-like Coatings for Orthopaedic Applications, Surface Modification Technologies, 1992, p.125.

[9] J. Davidson, A. Mishra. Surface Modification Issues for Orthopaedic Implant Bearing Surfaces. Proc. 5th Int. Conf. Surf. Modification Tech., Inst. of Metals, London, 1992, and J. Mater. & Mfg. Proc., Marcel Dekker, Inc., N.Y., 1992.

[10] J.C. Haygarth and L.J. Fenwick. Improved wear resistance of zirconium by enhanced oxide films, Thin Solid Films 118 (1984), p. 351-362.

[11] P. Kumar, M. Oka, K. Ikeuchi, K. Shimizu, T. Yamamuro, H. Okumura, and Y. Kotoura, Low wear rate of UHMWPE against zirconia ceramic (Y-PSZ) in comparison to alumina ceramic and SUS 316L alloy, Journal of Biomedical Materials Research 25 (1991), p. 813-828.

[12] S.E. White, L.A. Whiteside, D.S. McCarthy, M. Anthony, and R.A. Poggi, Simulated knee wear with cobalt-chromium and oxidized zirconium knee femoral component, Clinical Orthop. 309 (1994) p. 176-184.

[13] H. Oonishi, M. Aono, N. Murata, and S. Kushitani, Alumina versus ppolyethylene in total knee arthroplasty, Clinical Orthop. 282 (1992) 95-104.

[14] B. Derbyshire, J. Fisher, D. Dowson, C. Hardacker, and K. Brummit. Comparative study of the wear of UHMWPE with zirconia ceramic and stainless steel femoral heads in artificial hip joint, Med. Eng. Phys. 16 (1994), p. 229-236.

[15] V.O. Saikko. Wear of the polyethylene acetabular cup: the effect of head material, head diameter, and cup thickness studied with a hip simulator, Acta Orthop. Scand. 66 (1995) p. 501-506.

[16] B. Cales, Y. Stefani, E. Lilley. Long-term in vivo and in vitro aging of a zirconia ceramic used in orthopaedics, J. Biomed. Mat. Res. 28 (1994) 619-624.

[17] P. Christel, A. Meunier, M. Heller. Mechanical properties and short-term in vivo evaluation of YPSZ, Journal of Biomedical Materials Research, vol. 23 (1989), p. 45-61.

[18] P. Kovacs, J. Davidson, Effects of the electrochemical behaviour of implant metals on osteoblast and oral bacterial adhesion, Orth. Research Societies Meeting (1995), p.226

[19] S. Goodman, J. Davidson, V. Fornasier, A. Mishra. Histological response to cylinders of a low modulus titanium alloy and a wear resistant zirconium alloy implanted in the rabbit tibia, Journal of Applied Biomaterials, Vol. 4 (1993), p. 331-339.

[20] T. Albrektsson, H. Hansson, B. Ivarsson, Interface analysis of titanium and zirconium bone implants, Biomaterials 1985, vol. 6, p. 97.

[21] A. Patel, M. Spector, Oxidized zirconium for hemiarthroplasty: an *in vitro* assessment. Bioceramics, Vol. 8 (1995), p. 169.

[22] S. Newcomb, D. Foord. Instabilities in the oxidation behaviour of Zircalloy-4, Microscopy of Oxidation 2, Institute of Materials, London, 1994, p.374.

[23] R. Ploc, S. Newcomb. Porosity in zirconium oxide films, Microscopy of Oxidation III, Institute of Materials, London, 1997, p.475.

[24] Y. Lin. Nature of oxidized β-phases in Zr-2.5Nb alloy, Microscopy of Oxidation III, Institute of Materials, London, 1997, p.462.

[25] L. W. Hobbs, M. Treska, V. Benezra and S. Mangin, Oxidized Zirconium Alloy Oxidation Microstructures and Interfaces in Prosthetic Applications Investigated using Transmission Electron Microscopy, Internal report, Smith & Nephews Inc., (Memphis, TN), Sept. 1997.

[26] F. Garzarolli, H. Seidel, R. Tricot, and J. P. Gros. Oxide growth mechanism on zirconium alloys. Zirconium in the Nuclear Industry: Ninth International Symposium, (ASTM, Philadelphia, PA, 1991), p.395-415.

[27] J. Godlewski, J.P. Gros, M. Lambertin, J. F. Wadier and H. Weidinger. Raman spectroscopy study of the tetragonal-to-monoclinic transition in zirconium-oxide scales and determination of overall oxygen diffusion by nuclear microanalysis. Zirconium in the Nuclear Industry: Ninth International Symposium, (ASTM, Philadelphia, PA, 1991), in: ref.6, p.416-36.

[28] B.A. Cheadle and S. Aldrige. The Transformation and Age hardening behaviour of Zr-19wt%Nb. Journal of Nuclear Materials, 1973, v47, p. 255.

[29] O.T. Woo, D.J. Lockwood, Y.P. Lin and V.F. Urbanic. Structure of Oxides grown on Zr-20Nb alloy. Mat. Res. Soc. Proc., 1995, v357, p. 219-224.

[30] I. J. McColm. Ceramic hardness. Plenum Publ., 1990.

[31] P. Kofstad. Oxidation of Zirconium, High Temperature Corrosion, 1988, p.299.

[32] M. Hansen, K. Anderko. Constitution of binary alloys, McGraw-Hill, 1958, p. 1023.

[33] R. S. Roth, L.W. Coughanour. Phase Equilibrium Relations in the Systems Titania-Niobia and Zirconia-Niobia, J. Research, Natl. Bur. Standards, vol. 55, 1955, p.212.

[34] T. B. Reed, Free Energy of Formation of Binary Compounds, MIT Press, 1971.